DISTRIBUTION OF WORKING FLUID PHASES IN A HEAT PIPE

by

Kevin Laux

B.S. in Mechanical Engineering, University of Pittsburgh,

Pittsburgh, USA, 2014

Submitted to the Graduate Faculty of

the Swanson School of Engineering in partial fulfillment

of the requirements for the degree of

Master of Science

University of Pittsburgh

2015

UNIVERSITY OF PITTSBURGH

SWANSON SCHOOL OF ENGINEERING

This thesis was presented

by

Kevin Laux

It was defended on

December 1, 2015

and approved by

Laura Schaefer, Ph.D., Chair, Department of Mechanical Engineering, Rice University

Sung Kwon Cho, Ph.D., Department of Mechanical Engineering and Materials Science

Sangyeop Lee, Ph.D., Department of Mechanical Engineering and Materials Science

Thesis Advisor: Laura Schaefer, Ph.D., Chair, Department of Mechanical Engineering, Rice University

DISTRIBUTION OF WORKING FLUID PHASES IN A HEAT PIPE

Kevin Laux, M.S.

University of Pittsburgh, 2015

A unique experimental setup was designed with the aim of visualizing the behavior of working fluid phases, in an environment similar to a micro heat pipe. During experiment, deionized water and isopropyl alcohol, at varying fill ratios, were used as working fluids and video and temperature data were recorded over a range of input powers from 0 to 5 Watts. The effects of working fluid material properties and heat pipe fill ratio on thermal performance and phase distribution were investigated. An attempt was made to connect qualitative impressions from video images and with quantitative data collected through temperature measurement.

TABLE OF CONTENTS

LIST OF TABLES

LIST OF FIGURES

1.0 INTRODUCTION

The goal of this project was to gain an understanding of the interaction between the phases of a working fluid in a heat pipe. Parameters of interest were the fill ratio, or the percentage of the volume occupied by the working fluid, and the material properties of the working fluid. Many studies can be found measuring the effects of the parameters of interest on the performance of a heat pipe. However, there appears to be a gap in the literature concerning the interaction between working fluid phases, and their distribution, during heat pipe operation.

1.1 MOTIVATION

The background motivation for this work is the validation of a proposed lattice Boltzmann simulation concerning micro fluid phenomena in a heat pipe. Initially, previous work, as discussed in the literature, was planned to be used for this validation. However, when the literature was found to be lacking in observations of interaction between phases and the wicking material in a micro heat pipe, this investigation was started. In this chapter, the proposed study will be placed into the context of the larger challenges and accomplishments of the heat pipe and multiphase flow research communities. First, heat pipe design and operation will be briefly discussed. Next, an overview of multiphase flow will be presented. Differences in large- and small-scale flow regimes will be illustrated, as well as between different flow orientations and geometries. Finally, the lessons learned from these studies will be applied to the design and construction of the test sections to be used in this study.

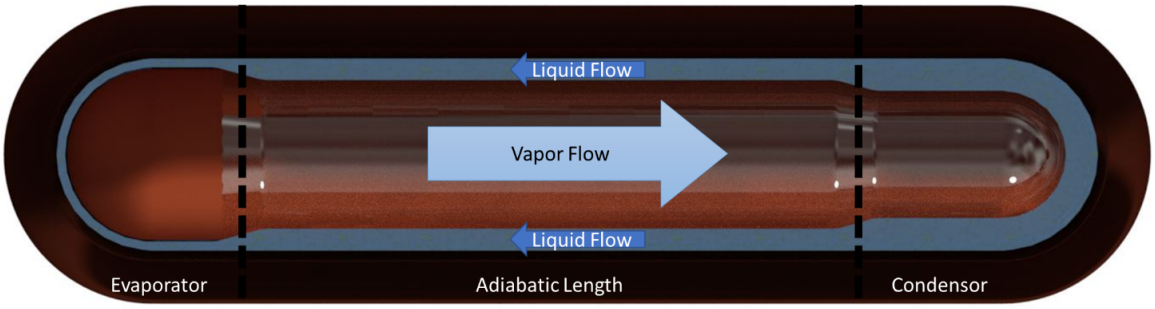

Figure 1: Illustration of a heat pipe.

1.2 HEAT PIPE BACKGROUND

A heat pipe is composed of a closed tube, with a wicking structure lining its inner diameter. The interior volume of a heat pipe is partially filled with a working fluid. When a heat flux is applied across the length of the tube, the working fluid evaporates at the warmer end of the tube and travels to the cooler end of the tube, where it condenses. The length of heat pipe between the evaporator and condenser is called the adiabatic length, and it is assumed that there is little, or negligible, heat transfer along this length. The vapor flow is driven by pressure differences due to phase change within the fluid. Depending on the orientation of the heat pipe, density differences between phases may also assist the flow of phases within the heat pipe. In this way, the heat energy required to change the phase of the fluid is transported along the heat pipe. The wicking material enhances phase change by increasing surface area, and returns the liquid to the evaporating section of the heat pipe via capillary forces. The two phases are in counter-flow, with only a two-phase interface between them. An illustrative schematic is presented in Fig. 1.

Heat pipes offer vastly increased heat transfer performance over simple conductors, because energy is transferred though fluid flow, a faster mechanism than conduction. Additionally, the temperature drop across the heat pipe is much lower because the working fluid exists at a near saturation condition, and the majority of the heat energy is transferred by

phase change, which does not involve a large fluid temperature change. Heat pipe performance can be measured in terms of both the thermal resistance and heat transfer coefficient, as presented by eqns. 1.1 and 1.2, respectively. The thermal resistance, R, is expressed in terms of heat input Q, condenser temperature, T_c, and evaporator temperature, T_e, such that:

$$R = \frac{T_e - T_c}{Q}. \tag{1.1}$$

The heat transfer coefficient, h, of a heat pipe is expressed as the heat input per unit area and temperature difference such that:

$$h = \frac{Q}{A(T_e - T_c)}. \tag{1.2}$$

where the temperature drop, $(T_e - T_c)$, is measured between the evaporating and condensing sections of the heat pipe, and the area, A, is taken as the cross sectional area of the heat pipe [1].

1.2.1 Heat Pipe Geometry

The geometry of the wicking material is very important to both the operation and performance of the heat pipe. If the wicking material is unable to return the condensed liquid to the evaporator quickly enough, dry out occurs. Dryout is a condition that occurs when the only vapor is present in the evaporator, and heat must be conducted along the heat pipe wall before reaching the liquid to evaporate. At this point, mass flow through the heat pipe stops increasing[2]. This adds a conductive thermal resistance and reduces heat transfer performance. Depending on the orientation of the heat pipe, the capillary pressure associated with the wick may become important to move the liquid phase against gravity. Past studies comparing wick types and geometries have found a geometry made of long axial grooves was best at transporting heat[1]. Additionally, for grooved wick types, the heat pipe's angle of inclination was found to have little effect on heat transfer performance[1]. Grooved heat pipes were also found to have the shortest time to reach equilibrium, when compared to other wick structures[3]. Additionally, it was noted that heat pipes exposed to larger heat loads

took longer to reach thermal equilibrium, as would be expected[3]. Other studies found that decreasing the feature size of the wick geometry improved the capillary pressure[2]. Wick structures with higher capillary pressure are less influenced by orientation, because they can carry liquid further against gravity. However, a smaller feature size increased friction in the wicking material, meaning that viscous effects must be considered, and lowered the mass flow rate of liquid through the wick[2].

1.2.2 Heat Pipe Working Fluid

The percentage of the heat pipe volume that is filled has also been found to have an effect on heat pipe performance. The fill ratio is measured as the percentage of the evaporator volume, which is the section of the heat pipe where the thermal load is applied. It has been found that there is an optimal fill ratio, and that a higher or lower fill ratio will lower heat pipe performance. Generally, increasing the fill ratio will improve heat pipe performance, until a maximum performance is reached. Further increasing the fill ratio past this point results in decreased thermal performance[4]. However, the performance at higher fill ratios is greater than that at lower fill ratios. Between studies, optimum fill ratios varied, suggesting geometry dependence[4, 5, 6] . Additionally, the optimal fill ratio appears to vary with different working fluids[4, 5, 6]. Working fluid saturation temperature is an important material property in heat pipe operation. If the saturation temperature of the working fluid is not achieved, phase change will not occur, and heat transfer performance will be diminished[7]. The effect of saturation temperature can be removed by manufacturing the heat pipe such that the working fluid inside is at saturation. This is achieved by evacuating the volume, so that only working fluid is present. Other studies investigating heat pipes partially filled with different working fluids showed similar results. Badran et al., compared the performance of methanol and water at different fill ratios[6]. These working fluids were investigated in an array of triangular microchannels, with a width of 100 micrometers and a length of 2.54 cm. Fill ratios of 5% and 20% of the total volume were tested to find the effect of thermal conductivity. The results of this study are shown on the following page in Fig. 2.

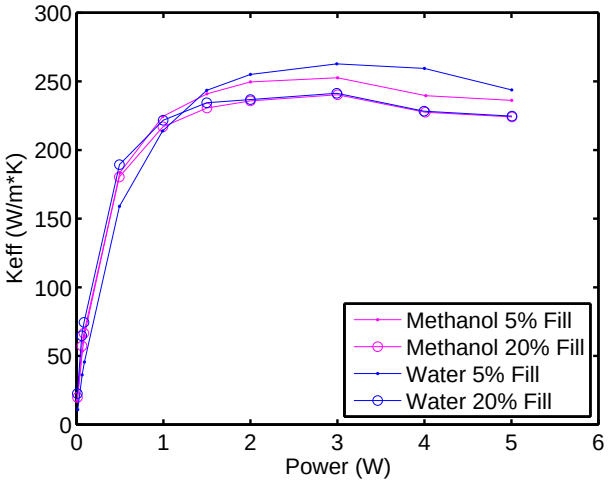

Figure 2: The effect of fill ratio and working fluid on thermal conductivity from Badran et al.[6]

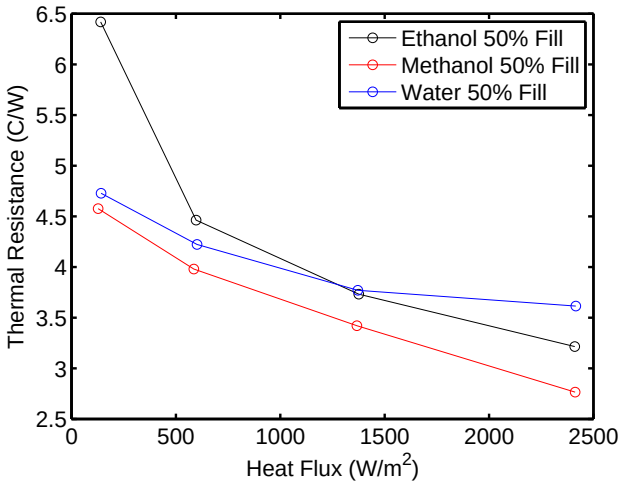

Figure 3: The effect of working fluid on thermal resistance compiled from Peyghambarzadeh et al.[8]

The data show that water is more effective than methanol at lower fill ratio. However this performance advantage disappears for the 20% ratios, especially at higher input powers, as seen in Fig. 3. Peyghambarzadeh et al., investigated the effect of water, methanol and ethanol on thermal resistance in a heat pipe with a diameter of 1.905 cm[8]. A fill ratio of 50% of the evaporator was used for all working fluids. Methanol was found to be superior to ethanol and water for all heat fluxes. As heat flux increases, the reduction in thermal resistance decreases, most notably when water is used as a working fluid.

1.3 MULTIPHASE FLOW BACKGROUND

Several efforts have been made to define the length scale at which microscale behavior begins for multiphase flows. The primary motivation for investigation of flow regimes at smaller scales is the development of smaller, high powered devices, coupled with the need to cool these devices, often with microflow channels. Multiphase flows, and therefore also the associated heat transfer mechanisms, behave differently at these scales, motivating the development of criteria to define the microscale. To this end, several dimensionless numbers have been proposed and examined. Triplett et al.[9] proposed the use of the Laplace constant, L, defined in egn. 1.3, as an upper bound for the order of magnitude at which channel diameters could be considered microscale. The constant is the ratio between the surface tension forces between phases and the difference in magnitudes of the body forces acting on the phases:

$$L = \sqrt{\frac{\sigma}{g(\rho_l - \rho_g)}}. \tag{1.3}$$

where σ is the fluid surface tension, ρ_g and ρ_l are the densities of the gas and liquid phases of the fluid, respectively, and g is the gravitational constant. The confinement number, Co, has been proposed as a modification of the Laplace constant. The number, defined in eqn. 1.4, includes the hydraulic diameter of the tube, D_h:

$$C_o = \frac{1}{D_h}\sqrt{\frac{4\sigma}{g(\rho_l - \rho_v)}}. \tag{1.4}$$

A further criterion was developed using a linear stability analysis of a stratified flow [10]. This analysis argued that stability needed to consider a disturbance wavelength of the same magnitude of the tube diameter. The Eötvös ($E\ddot{o}$) number, which is a formulation of the Bond (Bo) number, is defined in eqn. 1.4. The reciprocal is used to reflect the dominance of surface tension at these scales, with a proposed critical value.

$$E\ddot{o} = \frac{(2\pi)^2\sigma}{(\rho_l - \rho_g)D_h^2 g}. \tag{1.5}$$

There is poor agreement between these criteria for several saturated fluids when plotted against reduced pressure. Kandlikar proposed a range from 200 μm to 3 mm; however, there is no consensus in the literature[10]. This has caused much dispute over the bounds used to define the microscale, although all criteria proposed agree that differences in flow behavior, between micro and macroscales, are governed by a balance between body and surface tension forces. This section will examine studies on tubes with diameters of 3 mm or less, in an attempt to gain an understanding of both reasonable criteria and the behavior of flows at these scales. An important tool in the investigation of flow behavior is the flow regime map, which identifies flow regimes on a plot of superficial gas and liquid velocities, in an effort to show transitions between flow regimes in terms of superficial liquid and gas velocities.

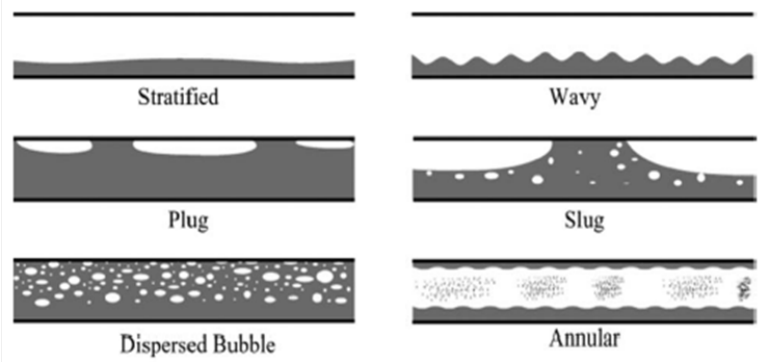

Figure 4: Horizontal multiphase flow regimes.[10]

1.3.1 Horizontal Multiphase Flow

At the macroscale, horizontal multiphase flows are often separated due to the difference in density, and therefore gravitational forces, between the individual phases. The interaction of this body force and surface tension between phases at different liquid and gas flow rates leads to the regimes or patterns depicted in Fig. 4 [10]. The flow regimes most influenced by gravity at these scales are stratified and wavy flows, in which the phases are completely separated, with the gaseous phase in the top portion of the tube, and the liquid phase occupying the bottom section. As tube diameter decreases, the dimensionless numbers mentioned in the previous section suggest a diminished influence of gravitational body forces and the disappearance of these flow regimes. Several papers have been reviewed in order to investigate the reduced effect of gravity at smaller tube diameters on flow regime maps. At the lowest superficial gas and liquid velocities, bubbles much smaller than the diameter of the channel they occupied were observed. As the superficial gas velocity was increased, bubbles were observed to coalesce at the top of the channel and form slugs of approximately the channel diameter. As gas velocity was increased, or liquid velocity was decreased, longer gas slugs and shorter liquid slugs were observed. It was noted that the liquid film above the gas slugs was slightly thinner than the film below the slugs. When further increasing the superficial gas velocity, tiny gas bubbles appeared in the liquid slugs. Increasing the superficial liquid velocity from this state leads to a transition to churn flow. Annular flow was achieved by increasing the superficial gas velocity from the slug flow state. Liquid waves seen in annular flow became smaller in amplitude as superficial gas velocity was increased. Triplett et al. were unable to observe stratified flows under any condition [9]. Although no critical value above which this regime is impossible was suggested, it was noted that for all geometries tested, $Eö \geq 100$. Other studies have been able observe stratified flows, but only at superficial gas velocities an order of magnitude lower, and superficial gas velocities an order of magnitude higher, than the range used in this study. Flow regime maps from both diameters investigated have been combined in Fig. 5 for comparison[9].

From Fig. 5, the following conclusions about the effect of decreasing tube diameter on flow regime transitions can be drawn. Transition from slug-annular to annular occurs

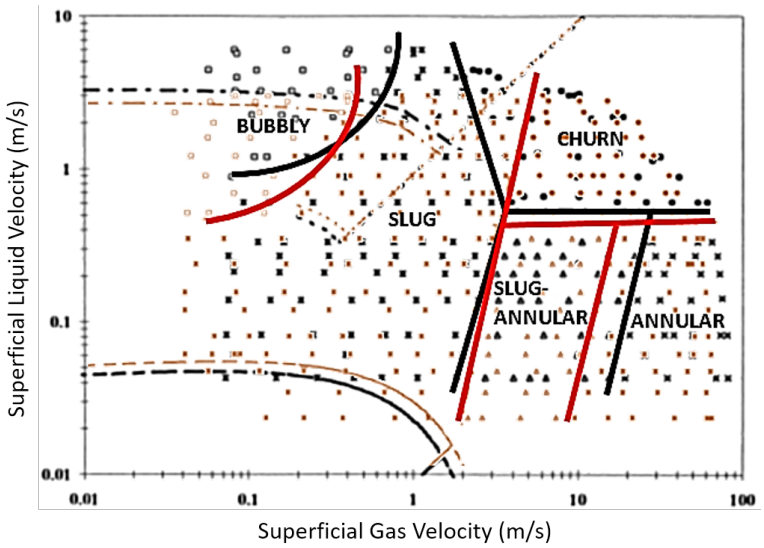

Figure 5: Flow Regime Maps for 1.097mm (black) and 1.45mm (red) tube diameters adapted from Triplett et al.[9]

at a higher superficial gas velocity, while transitions between slug and slug-annular flow, and churn and annular flow occur at similar superficial gas and superficial liquid velocities, respectively. At high liquid velocities, the slug regime between bubbly and churn flows covers a smaller range of superficial gas velocities. Interestingly, the plug flow regime referenced in Fig. 4 is not present in this flow regime map. It is mentioned that the regimes identified as slug and slug-annular in this study have been labeled as plug, and slug, respectively, in other studies. Yang and Shieh[11] conducted experiments on air-water and R-134a two-phase flows in horizontal tubes with diameters from 1 to 3 mm. They proposed to observe the effect of surface tension between the gas and liquid phase of the flow, as the surface tension forces between air and water (72 mN/m) are much greater than those between liquid and vapor R-134a (7.5 mN/m). Flow regimes maps for both fluid combinations are compiled and shown in Fig. 6. In water-air flows, Yang and Shieh encountered bubble, plug, slug, dispersed, slug-annular and annular flow regimes, in addition to, at larger tube diameters, a wavy flow pattern. As can be seen in Fig. 6, the wavy flow regime becomes smaller with decreasing

tube diameter, until it disappears in the 1 mm flow regime map. Transitions from bubble to dispersed regimes, and from slug-annular to annular, in addition to the critical superficial liquid velocity, remain generally the same across tube diameters. The difference in size of the slug-annular regime may be due to the difficulty of identifying flow transitions in air-water flows. The critical liquid superficial velocity is similar to results from Triplett et al., in Fig. 5. Transition between plug and slug flows is seen to occur at higher superficial gas velocities, with decreasing tube diameter.

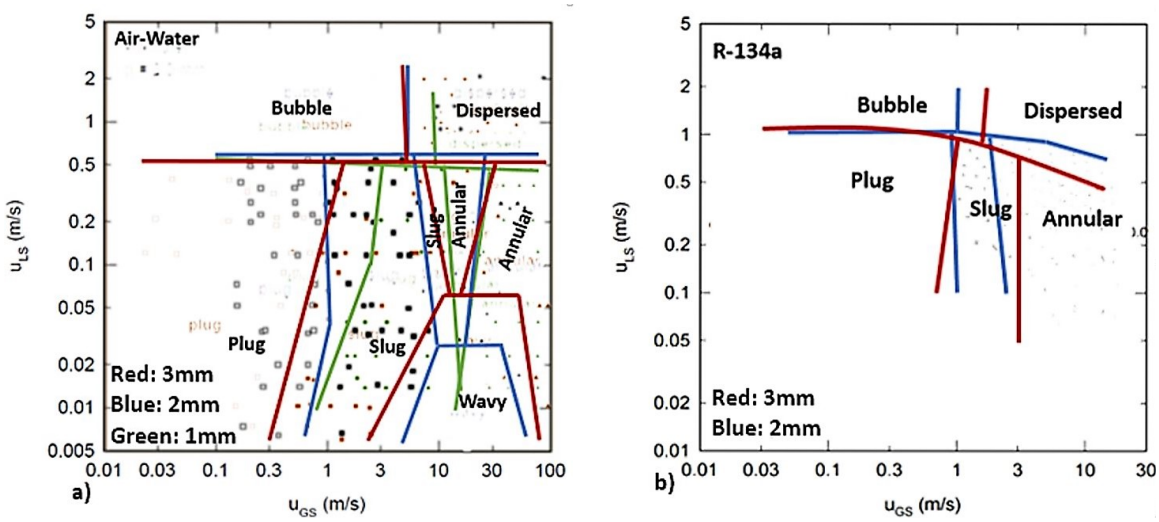

Figure 6: Flow Regime Maps for Air-Water (left) and R-134a (right) adapted from Yang and Shieh.[11]

The size of the wavy flow regime can clearly be seen to shrink with decreasing tube diameter. As the minimum liquid velocity, for the 1 mm test cases, was 0.014 m/s, very nearly approaching zero, it could be suggested that wavy flows are impossible at a 1 mm tube diameter. A flow regime map comparison for R-134a flows studied by Yang and Shieh is provided in Fig. 6b. It was noted that transitions between flow regimes were much easier to determine for R-134a than for air-water flows. The lack of a slug-annular regime is explained by these clearer transitions. As with air-water flows, the size of the slug regime was reduced with decreasing diameter. The transition between bubble and dispersed flow also appears to occur at lower gas velocities. A critical liquid superficial velocity line across tube diameters,

as seen in Fig. 5 and Fig. 6a, is not present in the R-134a flow regime maps. It is unclear whether or not this is due to the reduced surface tension forces in R-134a, or phase change caused by different heat transfer characteristics at higher flow rates and larger tube surfaces areas. Unfortunately, a flow regime map for a 1 mm tube diameter is not provided. A further reduction in diameter would allow for suggested trends with decreasing diameter to be confirmed. Comparing the plots in Fig. 6, in general, transitions for R-134a flow occurred at higher liquid velocities and lower gas velocities, than those for air-water flows. Yang and Shieh posit that this shift in flow transitions is due to lower surface tension, allowing bubbles to coalesce and liquid coverage across the tube diameter to be broken sooner. A lowered resistance to transition between flow regimes may cause transitions to occur over a smaller range of superficial velocities, making them easier to identify. Interestingly for a constant tube diameter, regardless of working fluid, the transition from plug to slug flow appears to occur at the same superficial gas velocity. Although difficult to confirm from a comparison of only two fluid combinations, this could be an interesting phenomenon for future study. Coleman and Garimella examined air-water flows through horizontal glass with diameters of 1.3, 1.75, 2.6, and 5.5 mm [12]. Superficial liquid and gas velocities were varied between 0.01-10 and 0.1-100 m/s, respectively. Blue dye was mixed with the water to aid in flow visualization, though of course this slightly alters the expected fluid properties. An effort was made to adopt a consistent naming system, through the definition of four flow regimes: stratified, intermittent, annular, and dispersed. These regimes were further divided into patterns: stratified smooth and stratified wavy, plug and slug, wavy annular and annular, and bubble and dispersed, respectively. The resulting flow regime map comparing all tube diameters is included in Fig. 7.

As with previously examined studies, the stratified regime shrinks and disappears with decreasing tube diameter. The difference between macro-and microscale flow behavior is clearly seen by the inclusion of the 5.5 mm diameter tube. Transitions for the three smaller tube diameters are almost identical by comparison, and can be examined and compared to previous studies. Contrary to results obtained by Triplett et al. [9], and Yang and Shieh [11], the liquid velocity at which transition to the dispersed regime occurs increased with decreasing diameter, instead of remaining constant. With decreasing tube diameter,

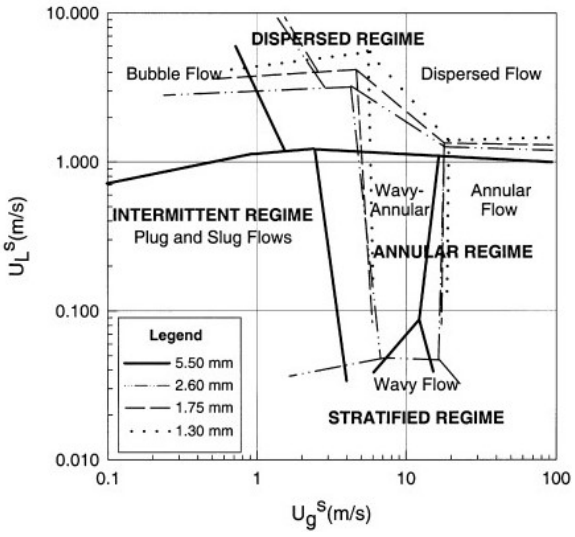

Figure 7: Air-Water Flow Regime Map from Coleman and Garimella.[12]

transitions between intermittent and annular regimes, as well as within the dispersed regime, occur at higher gas velocities, a trend supported by both studies. As noted above, the effect of the dye on the fluid properties in the water was not incorporated, but this could be relevant if it changed the fluid's surface tension.

1.3.2 Vertical Multiphase Flow through Micro Tubes

Vertical multiphase flow is similar to horizontal multiphase flow, except that due to the change in orientation, the effect of gravity on the flow is negligible. Without the separating effects of gravity, the flow patterns are symmetrical across the tube diameter, and stratified flow regimes are not present. Despite the lack of gravitational effects, differences may still be seen between macro-and microscale geometry. Commonly seen vertical flow regimes are included below in Fig. 8. Transitions between these regimes are similar to what is observed in horizontal flow and will be covered briefly. Bubbly flow occurs at the lowest superficial gas velocity, where increasing the gas superficial velocity will promote bubble coalescence, and the flow will transition to slug flow. Increasing both liquid and gas velocity leads to a flow

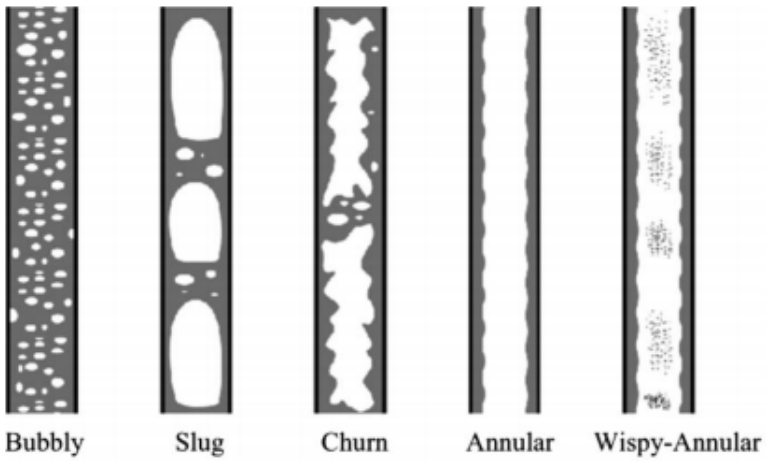

Figure 8: Flow regimes for vertical flow. [13]

regime known as churn flow, a highly unstable flow regime with large bubbles with jagged edges. Further increasing the superficial gas velocity causes the bubbles in the channel center to merge together, leaving only a thin layer of liquid on the inner circumference of the tube.

Mishima and Hibiki observed demineralized water and air flows in vertical glass tubes with diameters of 1.05, 2.05, 3.12, and 4.08 mm [13]. The aim of their study was the investigation of models that proposed transition lines between flows. The study also measured void fraction of the flow through neutron beam attenuation; however, this was not used to determine flow regime transitions. Mishima and Hibiki were able to observe differences in the flow regimes between the largest and smallest diameter pipe. Sketches of these regimes are included below in Fig. 9, with small diameters denoted by an asterisk.

For the smallest tube diameters, bubbly flows featured bubbles concentrated along the tube axis. As these bubbles grew, they formed trains of bubbles the same diameter as the tube which coalesced into long slugs to complete the transition to slug flow. In slug flows, gas slugs were seen to have rounded spherical noses in the direction of flow, with tiny bubbles interspersed in the liquid slug that followed. Smaller tube diameters were observed to have much longer bubble slugs than larger diameters. As the flows transitioned to churn, the rounded bubble noses disappeared and the size and number grew of liquid bubbles

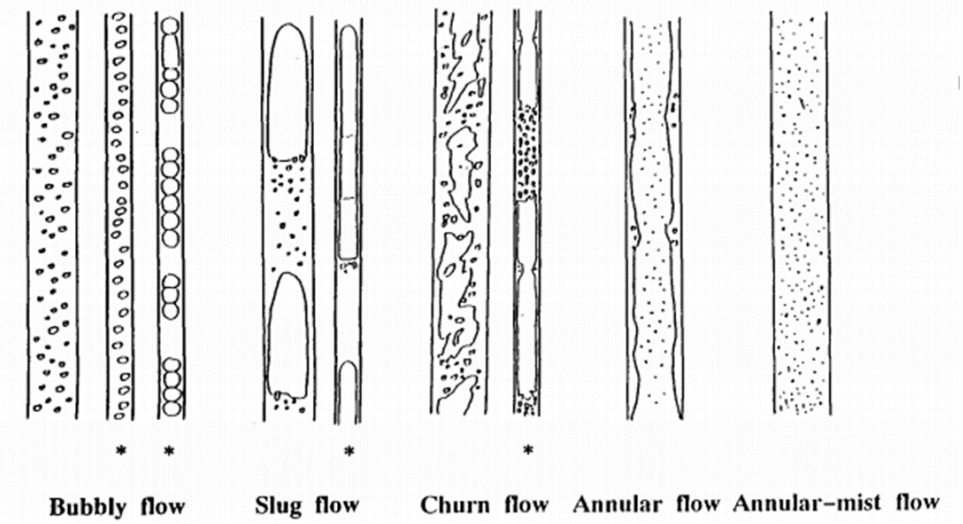

Figure 9: Flow regimes as identified by Mishima and Hibiki.[13]

interspersed in the liquid slugs. Flow regime maps are compiled and provided for 2 mm and 4 mm tube diameters; however, there are much fewer data points when compared to plots provided by Triplett et al.[9], and Yang and Shieh[11]. The lower number of data points can be attributed to the relatively small range of superficial velocities examined by Mishima and Hibiki[13]. Due to fewer data points, transitions between flow regimes are relatively unclear, although researchers believed that the data collected was enough to qualitatively validate a model put forth by Mishima[13].

1.3.3 Multiphase Flow Through a Vertical Annulus

Julia et al.[14] investigated water and air flows through a vertical annulus with an inner diameter 19.1 mm and an outer diameter of 38.1 mm at superficial gas and liquid velocities of 0.01-30 m/s and 0.2-3.5 m/s, respectively [14]. Although the geometry examined in this study is macroscale, the findings of this study can be easily applied to a microscale geometry, because vertical flows do not have the stratifying effects of gravity. For annular flow, four different basic flow regimes exist: bubbly flow, cap-slug flow, churn flow, and annular flow.

Bubbly flow is characterized by the presence of bubbles interspersed in liquid, and it has been noted that this regime is not significantly different from bubbly flow through a vertical tube. Cap-slug flows are denoted by the presence of a higher density of bubbles in addition to larger bubbles formed by coalescence. Once larger bubbles grow to a diameter greater than the space between the inner and outer diameters of the annulus, they become deformed and distorted, and these bubbles are known as cap bubbles. Bubbles wrapping around the inside diameter, but unable to cover the circumference completely, may also form and are known as slugs. Because imaging is done radially, it is difficult to distinguish between these bubbles, and therefore they are considered part of the same flow regime. Churn flow occurs when the superficial gas velocity is further increased. Breakdown of liquid and gas slugs is a characteristic of this highly unstable flow regime. Churn flow through an annulus was also noted to be very similar to churn flows through vertical tubes. Finally, annular flow was observed as a liquid film on the inner and outer diameters with gas flow with entrained droplets in between. Axial-view and radial view sketches of the flow regimes, in addition to images from an experiment, are depicted below in Fig. 10.

Interestingly, the flow regime present at each combination of superficial velocities was evaluated through the use of a pre-trained neural network. The void fraction of the flow was measured as electrical impendence over time at three positions along the test section. A statistical analysis was performed on the signal, and the results fed into a neural network that was able to reduce the bias in flow regime identification and increase the objectivity of flow regime transitions determined by the study. Several neural networks were used in combination, to ensure that transitions between flow regimes were clearly realized. Julia et al.[14] stated that for a grouping of fifty neural networks, the creation of flow regime maps has a repeatability of 95%. Also, flow regimes were analyzed at three positions from each set of superficial velocities. As parameters neared transition between flow regimes, flow would transition downstream. This is likely due to a slight separation between the gas and liquid phases along the length of the vertical channel, increasing the void fraction downstream.

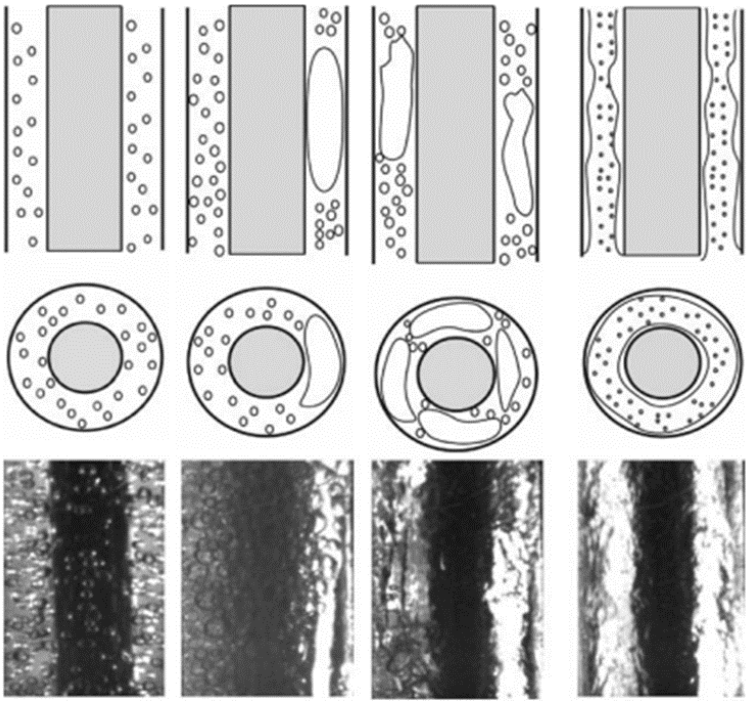

Figure 10: Vertical Annular Flow Regimes: Bubbly, Cap-Slug, Annular from Julia et al.[14]

1.3.4 Conclusions on Multiphase Flows

From the literature reviewed, it is clear that flow regimes and patterns are caused by a balance of surface tension, viscous, and gravitational body forces. Flow regimes were determined mainly by visual inspection, and occasionally with the assistance of an impedance-based void fraction measurement. From the observation of flows confined in smaller geometries, it is clear that the effect of gravity on the phases is diminished at smaller length scales. This statement is confirmed by the comparison of vertical flow regimes, where gravitational forces are axial, to flow regimes encountered in small-scale horizontal flows. The stratified flow regime, which is most affected by gravity, is missing from all of these test cases. Across all horizontal flow cases reviewed, it appeared that stratified flows were no longer present at tube diameters of 1.5 mm and below, since surface tension forces dominate over gravitational forces at small channel diameters. This suggests that microscale conditions for multiphase flow begins closely within the upper limit of the scale of 200 μm to 3 mm recommended by Kandlikar. Dimensionless numbers proposed as criteria for the transition to microscale behavior were unfortunately not evaluated by researchers for each test case, and a strong preference for defining test cases based on hydraulic diameter can be seen across all studies.

2.0 EXPERIMENTAL SET-UP

The information on multiphase full retimes in small-diameter channels outlined in Chap. 1 was used in the design of the experimental set up described in this following chapter. First, general design guidelines are determined in Sect. 2.1, while considering the manufacturing capabilities and budget available to the project, as shown in Fig. 11 and described in Sect. 2.2. A schematic of the experimental setup is shown in Fig. 11. After the components are discussed, the experimental procedure and the measurement devices used during experiment are presented in Sect. 2.3.

2.1 DESIGN GUIDELINES

The literature review in Chap. 1 informs several key points of the design. The conclusions drawn from the scale analysis in the multiphase literature reviewed led to a diameter that is

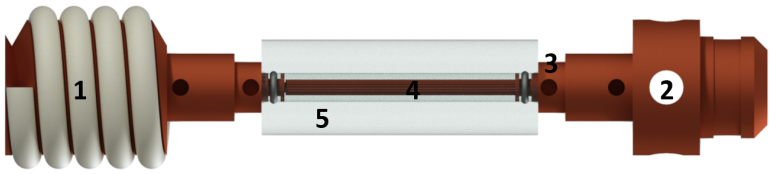

Figure 11: Experimental setup with numbered components. 1) Nichrome heating elements, 2.) copper cooling element, 3.) plug and o-ring, 4.) wick and 5.) borosilicate glass tube.

within the 200 μm to 3 mm range of diameters recommended by Kandlikar. In fact, observations from the flow regime maps reviewed and the geometries that led to the disappearance of any stratification favor a hydraulic diameter closer to the lower end of this range. In terms of orientation, vertical flow was found to behave most like microscale multiphase flow, regardless of hydraulic diameter. Furthermore, a grooved wick type was chosen based on the heat pipe literature, since a grooved wick's thermal performance was found to be independent of orientation, allowing results obtained from a vertical orientation, to be compared to a horizontal orientation. Visualization of phases within a heat pipe during operation is difficult, not only because the materials used in heat pipe construction are not transparent, but also because the inner diameter has a surface texture. This surface texture helps to wick liquid through the heat pipe and is where phase change occurs, making it an area of interest. However, the bottom-up view of the wicking material that would be offered by radial view of a fully transparent heat pipe would be inferior to a full view of this wick material. In an attempt to overcome these obstacles, it was decided that the experiment should mimic a heat pipe, by taking a radial slice of a heat pipe and inverting it. This is shown in Fig.12 below, with the arrows showing the orientations of the radial slices. This led to the core of the test section being composed of a wick surrounded by a volume of working fluid.

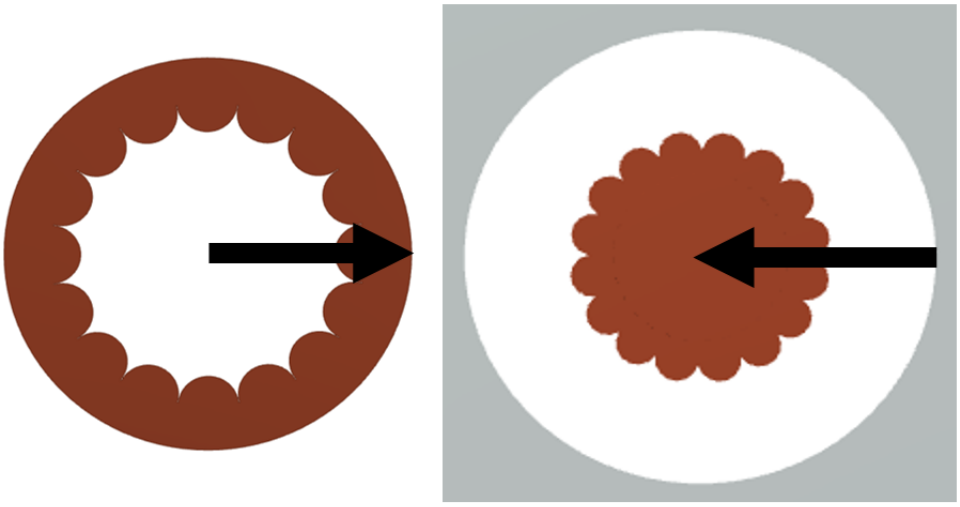

Figure 12: Radial Slices of a Heat Pipe (left) and Experiment (right).

In order for this change in orientation to be valid, it was important for the thermal boundary conditions on each end of the arrow that is superimposed on the figure to be preserved. This is somewhat simplified for the tip of the arrow, since the copper would conduct heat from one end of the heat pipe to the other, resulting in a similar temperature profile in both orientations (which could further be controlled by the mass of the copper, and the heat load). The boundary at the end of the arrow proved more difficult to replicate. In the image on the left, it was an adiabatic boundary, assuming symmetry. In order to approximate this boundary for the experiment, the outside of the experiment needed to be heavily insulated to prevent heat transfer. In a heat pipe, phase change occurs in the evaporator and condenser, where the heating and cooling loads are applied. Generally, these loads are applied radially to the copper. However, this was problematic to replicate in this case. Because of the small diameter of the copper wick, it was difficult to apply loads along a section of the centerline. Heating and cooling loads were applied axially to the wick instead. The size of the volume containing the working fluid around the wick was another important consideration. This volume was sized such that the ratio between the wick surface area and working fluid volume found in a heat pipe with similar wick surface area was considered. However, the diameter of this volume was made slightly larger, in order to approximate the distance between the wick surface and centerline. Two working fluids were chosen to investigate the effects of material properties on thermal performance and phase distribution. Deionized water and isopropyl alcohol were chosen as working fluids because of their availability and differing material properties of interest, which are tabulated in the table below. The chief properties of interest were the surface tension, viscosity, and the latent heat of vaporization, as these are thought to have the greatest impact on heat pipe thermal performance. Surface tension and viscosity are important in the movement of working fluid phases, and the latent heat of vaporization determines the amount of energy the working fluid is able to transport. In order to properly test the effects of these material properties and the fill ratio, the experiment was designed to be easy to disassemble and reassemble. This way, the same components can be reused for each trial, removing the effects of differing components, and allowing the effects of the fill ratio and working fluid alone to be evaluated.

Table 1: Material properties of working fluids.

Working Fluid	Surface Tension ($N \cdot m^{-1}$)	Latent Heat of Vaporization ($kJ \cdot kg^{-1}$)	Density ($kg \cdot m^{-3}$)	Viscosity ($mPa \cdot s$)
Water[15]	0.073	2442	997	0.89
Alcohol[16]	0.022	732	786	2.083

2.1.1 Test Section

For the purposes of this thesis, the assembly composed of components directly in contact with the working fluid are designated as the test section. The test section is composed of the wick, glass tube and two copper plugs that seal the tube ends, center the wick, and transfer heat to and from the wick. The volume contained by the test section was partially filled with the working fluid by a process described in Sect. 2.3.

2.2 COMPONENTS

This section will provide in-depth descriptions of each component. Component design choices and testing will also be discussed.

2.2.1 Heating Element

The heating element was constructed of a Nickel-chromium resistive wire wrapped around a threaded copper core and held in place with thermally conductive epoxy. The copper core was machined on a lathe from 0.5" Copper 145 stock rod. Copper 145 is a copper tellurium alloy that is easily machinable, and has thermal properties similar to pure copper. The relevant properties for comparison are shown in Tab. 2. When compared to pure copper, Copper 145 has a slightly lower thermal conductivity; however, it has much higher relative

Table 2: Material properties of copper alloys. [17]

Alloy	Percent Copper by Weight	Thermal Conductivity ($W \cdot m^{-1}K^{-1}$)	Relative Machinability
Copper 101	99.99	391	20
Copper 145	99.5	355	85

machinability. Relative machinability is a scale that allows for the machinability of materials to be compared, with brass being arbitrarily set to 100.

The core of the heating element was threaded, to increase the contact area between the wire and the core and to provide a guide for wire wrapping. Pelican Ni-Chrome resistive wire coated in PFA with a resistance of 0.887 Ω-ft and a nominal diameter of 0.1" was wrapped around the core. PFA insulation provided electrical insulation between the copper core and the individual loops of wire, to prevent short circuits. PFA insulation was chosen because of its excellent temperature resistance, up to 260°C. The core was dimensioned such that five full wraps of wire would fit along its length. During assembly, the wire was wound around a cylinder with a diameter slightly smaller than the pitch diameter, then the wire was removed from the cylinder, and the core was turned into wire. This processes ensured tight contact between the core and the wire. After assembly, the heating element had a measured resistance of 0.4 Ω at room temperature. AngstromBond 9123 was used to bond the NiChrome wire in place around the threaded core, as seen in Fig. 13. AngstromBond was selected because of the high strength bond it creates with both metals and plastics and its relatively high operating temperature range, up to 170°C. AngstromBond cures quickly at high temperatures. Therefore, because of its low viscosity, the epoxy was applied in thin coats at high temperature to obtain an even coat.

An extrusion at one end of the core allowed for the insertion of a 3/16" copper plug. The heat load was adjusted and monitored by a power supply, with a hole at the base of the extrusion allowing for heater temperature measurement close to the part centerline. The

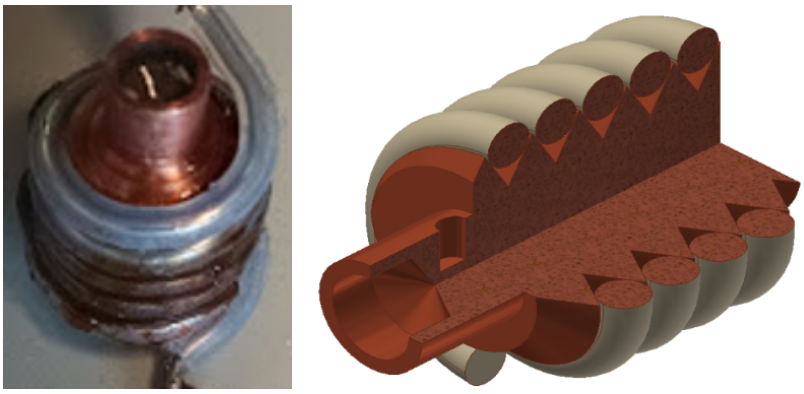

Figure 13: Heating element without insulation, finished (left) and solid model (right).

heating element is insulated through a combination of silicone ($\kappa \approx 0.1$ $Wm^{-1}K^{-1}$) and Styrofoam ($\kappa \approx 0.03$ $Wm^{-1}K^{-1}$) insulation. Initially, the heating element was insulated only by Styrofoam. However, after extended use, the Styrofoam in contact with the Ni-chrome wire had begun to warp and melt. Therefore, the decision was made to use a composite insulation, with a layer of silicone between the Styrofoam and the heating element. Although the silicone has a higher thermal conductivity than Styrofoam, its higher temperature resistance was better suited for direct contact with the Ni-Chrome wire. Additionally, silicone's flexibility made it well-suited for any stresses caused by thermal expansion of the heating element.

2.2.2 Cooling Element

The cooling element was made from the same Copper 145 stock as the heating element. General shaping and end hole operations were done with a lathe, while the radial holes were made using a milling machine. Cooling is provided by compressed air from a building supply line. Air enters the cooling element axially, impinges on the surface at the base of the end hole and then exits through four radial holes. Similar to the heating element, an extrusion opposite the impinged surface allows for the insertion of a copper plug, and a small radial hole at its base allows for temperature measurement. Air is supplied through a Tygon hose

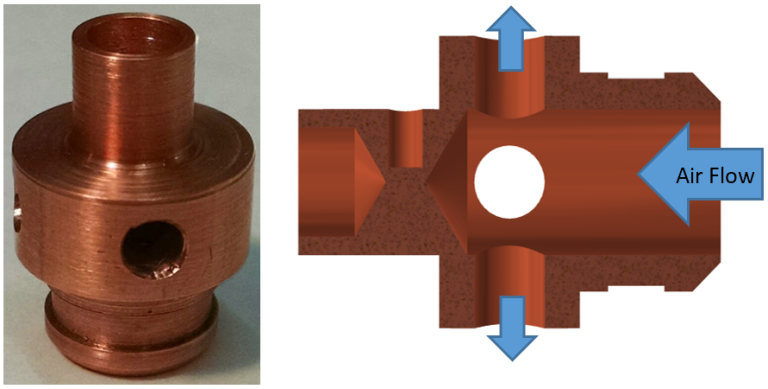

Figure 14: Cooling element: manufactured part (left) and solid model cross section (right).

fixed over the grooved feature machined into end of the cooling element. The air flow path is through the cooling element cross section, and the manufactured parts are shown in Fig.14. A valve at the building wall was used to control the flow of air. The air flow rate was measured by an FL7311 rotameter from Omega and temperature by a K-type thermocouple.

The cooling element and hose are held by an ABS part manufactured on a Makerbot Replicator 2X, shown in Fig. 15. ABS plastic was chosen over PLA because ABS has a higher glass transition temperature, making ABS less prone to deformation at high temperatures. The cooling element and hose are inserted through center hole, which narrows internally to compress the hose over the end of the cooling element and secure it. A slot in the side of the holder fits into a vice, which is used to put the experimental setup under compression. Holes drilled through the part allowed thermocouples to be routed and secured.

Air cooling was chosen over other methods, such as water cooling or an ice bath, because of the ease of setup and operation, in addition to the relatively low heat load that needed to be dissipated. Air cooling was assumed to provide more stable cooling element temperature than an ice bath, and water cooling would require a return line and drain.

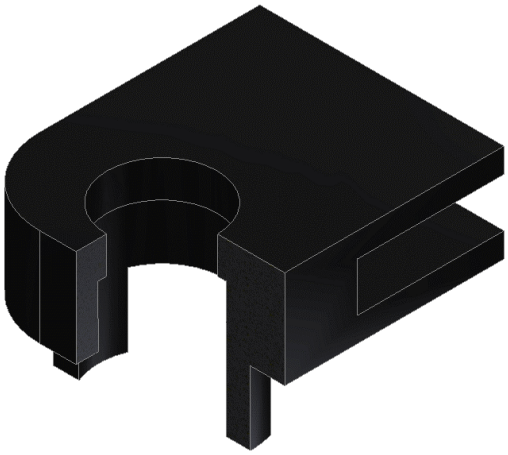

Figure 15: Solid model cross section of cooling element holder.

2.2.3 Wick

The wick was designed to emulate the wicking material found on the inside diameter of a grooved heat pipe. Due to the difficulty associated with accurate and repeatable machining of small surface features, the square grooves in the wicking material where mimicked by surface features made by 1 mm copper wire with sixteen 250 μm copper wires axially attached to its circumference.

Bare copper wires from Arcor Electronics with nominal diameters of 1.024 mm and 0.255 mm were used for this purpose, since wires of smaller diameter were found to be prohibitively difficult to work with. Prior to assembly, wires were straightened by stretching until failure. (Although they could be straightened initially, smaller diameter wires bent under their own weight, making them difficult to keep straight.) The straight wires were then cut to the correct length and assembled using the guide shown in Fig.17a, which allowed the 250 μm wires to be positioned around the 1 mm wire. The guide was made of two pieces of laser cut acrylic plate, one 0.5" thick piece with a 1/16" through hole, and one 0.25" thick piece with a 0.045" hole with a depth of 0.1". Both pieces had four edge holes in which dowels were placed to properly align the pieces. The thicker piece allowed for both the core and

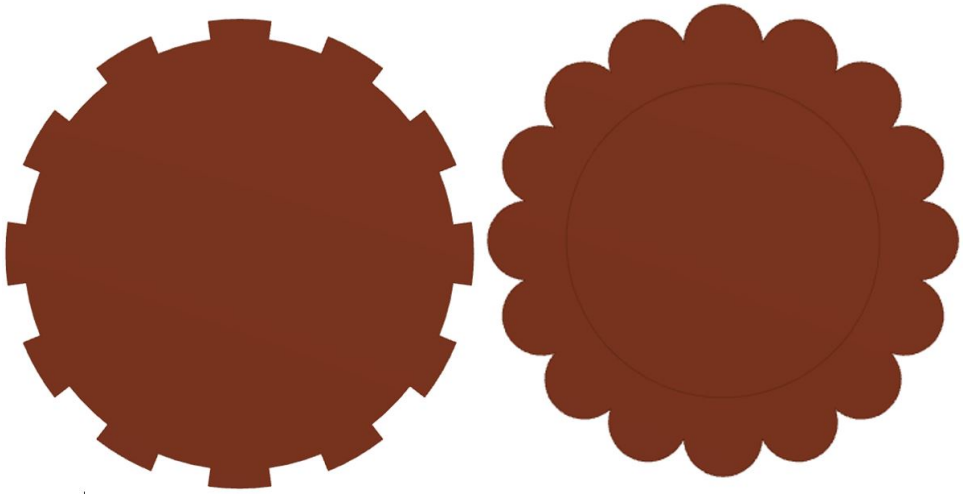

Figure 16: Wick profiles: ideal (left) and manufactured (right).

surrounding wires to be inserted, while the thinner piece only allowed the core wire to be inserted, creating an offset at the end of each wick, and ensuring that the surrounding wires were flush with each other. Once all of the wires were positioned correctly, the free end of the wick was wrapped in 250 μm wire to hold the wires in place. After removal from the guide, the opposite end of the wick was wrapped and the result was vacuum-sealed in a quartz tube, back filled with argon, for sintering. The quartz tube and wrapped wick are shown in Fig. 17b. Previous sintering attempts in an air environment resulted in undesirable reactions with the copper wick. The entire length of the wick was wrapped to prevent any sagging due to uneven support against gravity during sintering. The wires were sintered in a ThermoScientific Thermolyne FB1315M Benchtop Furnance at 950°C for three hours. Copper's melting temperature is 1,085°C, so the sintering temperature was selected to be close enough to the melting point for the wires to fuse, but not high enough that surface geometry of the wick would be affected. The sintering time was chosen after attempts of shorter duration showed a weak bond between the surface wires and the center core. After sintering, the quartz tube was broken and wrapping wire was peeled off. The finished wick is shown in Fig. 17c.

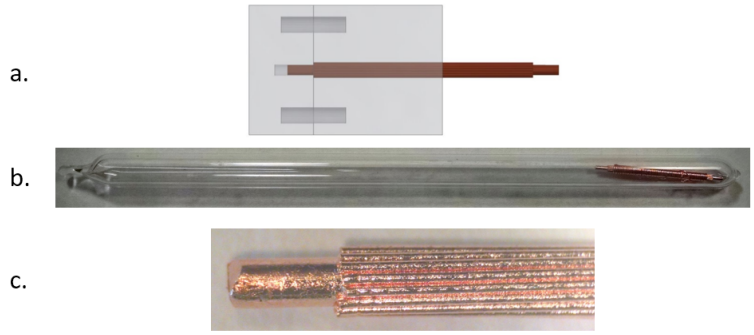

Figure 17: Wick construction: (a) solid model of the guide, (b) presintering (middle), and (c) finished wick.

The 1 mm wire protrudes at each wick end, allowing for insertion into the copper plugs. Once the wick was inserted into the copper plugs, silicone was applied to the interface to insulate the face of the plug and seal the interface between the wick and the plug. The silicone also covers any small differences in the lengths of the surface wires. The wick was manufactured to have an exposed length of 21.6 mm, giving it an aspect ratio (length to diameter) of about 14.

2.2.4 Copper Plugs

The copper plugs were machined on a lathe from the same Copper 145 stock as the heating and cooling elements. As mentioned previously, the plugs serve three main purposes: transferring heat to and from the wick, sealing both ends of the glass tube, and positioning the wick in the center of the glass tube. A finished plug and solid model cross section are shown in Fig. 18.

The body of the plugs was a 3/16" diameter feature that fits into the extrusions on the ends of both the heating and cooling elements, as pictured in Fig. 11. This was a loose fit, so good thermal contact between the plugs and the heating or cooling element was ensured through the use of thermal paste. Towards the top of the plugs, a radial depression allowed

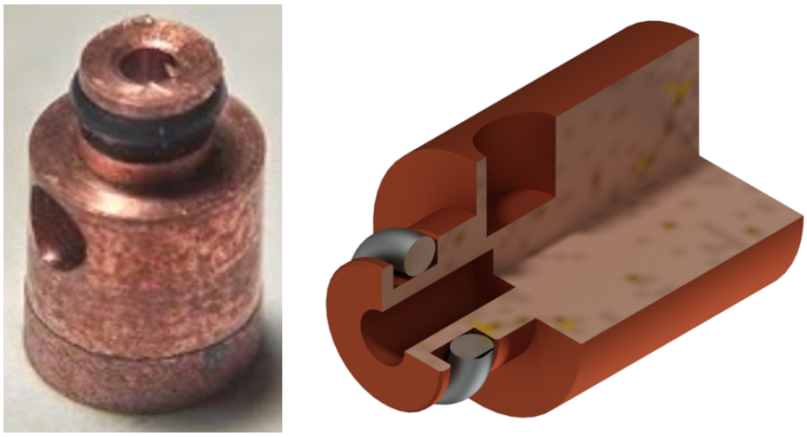

Figure 18: Copper plug: manufactured part (left) and solid model cross section (right).

for placement of a thermocouple reasonably close to the part center line. An extrusion from the main part body allowed for the plug to be fitted into the glass tube. Initially, the diameter of this extrusion was determined by a gauge pin measurement of the inside diameter of the glass tube. However, the accuracy achievable with the lathe was greater than that of the gauge pins. Therefore, the final plugs were machined to fit inside the glass plug, by removing material in 0.0002" diametrical increments and checking the fit after each increment. A variety of different seals between the plug and the glass tube were evaluated. The seal at this interface needed to be able to withstand the temperature change and the thermal expansion associated with operation. The seal would also have to be impermeable to gases to ensure only phases of the working fluid are present within the volume. The first seal attempted used a silicone sealant between the end of the glass tube and the body of the plug. This was quickly abandoned because of the cure time associated with silicone and its relatively high gas permeability. The 24 hour cure time meant that the seal would not be formed quickly enough to prevent leakage into and out of the volume. Once cured, silicone has a gas permeability two orders of magnitude higher than butyl rubber, and is not recommended for gas tight seals. Next another sealant was tested, Loctite 640. Loctite 640 is a high strength sleeve retaining compound the cures quickly in the presence of metal

ions. Unfortunately, Loctite 640 has a thermal expansion coefficient an order of magnitude higher than copper, and caused cracking in the thin walled glass tube initially used. To avoid cracking, two tubes with thicker walls were tested. The different wall thicknesses were tested through a thermal cycling test, which raised the temperature of the seal until water inside the tube boiled, and then air cooled the seal to ambient. After each wall thickness was cycled a total of three times, the tubes were illuminated from the opposite end to show any cracks that may have developed near the seal.

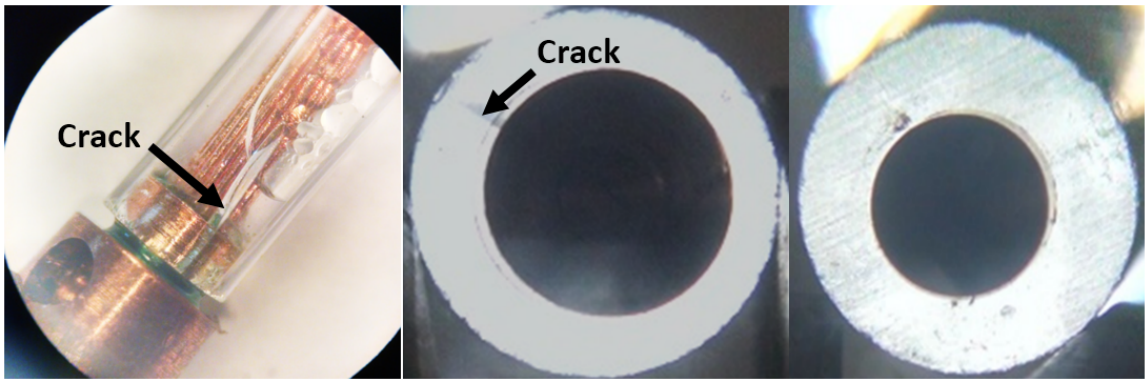

Figure 19: Wall thickness testing results: 0.835 mm (left), 2.15 mm (center) and 3.11 mm (right).

The results of this testing are shown in Fig. 19. From left to right, wall thicknesses of 0.835, 2.15, and 3.11 mm were tested by thermal cycling. The center and right images were illuminated and photographed axially, to make any cracking easier to see. Although a tube with a larger wall thickness stopped cracking due to thermal expansion, there were still several other problems with the Loctite seal. Loctite made a very high strength bond, and disassembly of the seal was only possible by breaking the glass tube. Also, preliminary tests using Loctite showed that the seal was unable to handle rapid changes in temperature. The sequence of images in Fig. 20 shows the failure of a Loctite seal as it is being cooled rapidly. On the left of each frame, an air bubble is clearly visible as it leaks into the test section.

Finally, a static, radial, micro O-ring seal was selected. An O-ring seal is quick to assemble, flexible during thermal expansion, and allows for easy dis-assembly. The seal consists of three parts, a piston (in this case the plug), a bore (the glass tube), and the

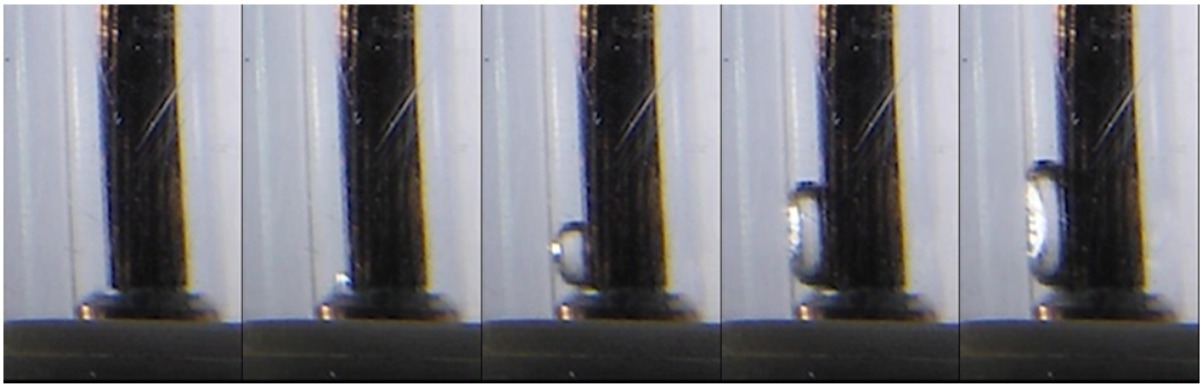

Figure 20: Loctite seal leaking with time increasing from left to right.

O-ring itself. The O-ring sits in a circumferential groove on the plug called the gland. The O-ring was both stretched by the diameter of this groove and compressed by the glass tube in order to form a tight seal. The width of this groove was dimensioned such that the O-ring had space to deform due to compression between the plug and the inner diameter of the glass tube. A smooth surface finish is recommended for a gas tight seal. As such, the diametrical face of the gland was machined removing the minimum amount of material possible, to create a polished surface finish. The inner diameter of the glass tube was assumed to be smooth enough. The gland determines the location of the seal, and for this reason it was moved as far towards the end of the plug as possible. Several different dimensions where tested before a 0.040" gland that started 0.010" from the end of the extrusion was chosen. This gland size was just wide enough to allow for O-ring compression, and a thinner front wall would be too easily deformed. The O-ring itself used in this investigation is micro O-ring made from Viton, or Fluorocarbon. Fluorocarbon has a large operational temperature range, -25°C to 230°C, and is rated for hard vacuum service, conditions well beyond those encountered in this experiment. The O-ring had a shore hardness of 75A, increasing its durability over more flexible options. A center end hole allowed the wick to be fit into the plug. This hole was sized to allow the exposed 1 mm wire at the each end of the wick to be fully inserted. To ensure full insertion, the hole depth is slightly greater than the length of exposed wire. A

small diametric clearance was left between the hole and wick end, to make sure that the wick end did not catch during insertion, which could cause bending of the wick. Thermal paste was used to decrease the thermal resistance across this clearance.

2.2.5 Glass Tube

As previously mentioned, a borosilicate glass tube with an outside diameter of 0.3515" and an inside diameter of 0.106" was chosen to contain the working fluid, and to provide a window for visualization. Borosilicate glass was selected because it is resistant to fracture due to thermal stresses. As previously stated in 2.2.4, this wall thickness was chosen to resist fracture due to the expansion of the copper plugs. A thicker wall has the added benefit of improving the insulation of the working fluid, as borosilicate glass has a relatively low thermal conductivity of 1.2 W/m·K.

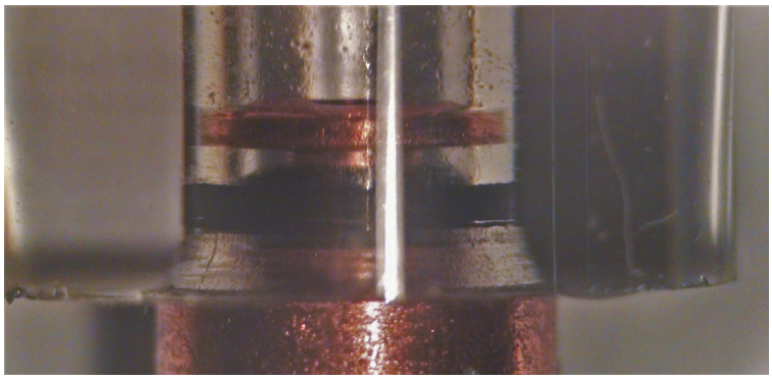

Figure 21: Borosilicate tube with chamfer and inserted copper plug with o-ring seal

Borosilicate glass presented several difficulties during assembly, particularly during O-ring insertion. The sharp edges on the inner diameter would shear the O-rings, instead of compressing them. This issue was resolved by grinding a lead-in chamfer of 15 degrees into each inner diameter. To do this, a specialized grinding tool was machined from an aluminum oxide grinding stone to have a 15 degree taper from the centerline. This grinding tool was then used in the end hole attachment on the lathe, at 3000 rpm. This allowed a chamfer to be created that was deep enough for the O-rings to be inserted without damage, but ended

before the beginning of the gland groove on the plugs. Generally, prior to assembly, the glass tube and O-ring were wetted with the working fluid for lubrication, to reduce the chance of O-ring shearing. The result is shown in Fig. 21.

2.2.6 Insulation

While conducting the previously mentioned thermal expansion tests on glass tubes of different thicknesses, an interesting phenomenon was noticed. During the test, a vapor blanket would fill the bottom of the tube. This blanket formed and collapsed periodically, pointing to an appreciable heat loss radially through the glass tube. In order to reduce this heat loss, the use of air gap insulation was investigated. The following images are stills of an insulation test. The purpose of the test was to observe the effects of an air-gap insulation, similar to the one shown in Fig. 22 on a periodic dryout behavior that was observed. The cycle begins with small bubbles forming quickly on the copper face, seen at three seconds and six seconds in Fig. 22. Once enough of the fluid has been heated, a large vapor bubble forms, inhibiting rewetting of the copper face. As this bubble grows, it loses energy to both the liquid above it and the walls of the glass tube. At a critical point, the bubble has cooled enough to return to the liquid phase and the cycle begins again. In this test, a tube a with wall thickness of 0.085" and an inner diameter of 0.106" had a copper plug sealed into it, using Loctite 640 epoxy. The copper plug, which had a flat face, was seated in the heating element, which supplied 3.5 Watts of power. A thermocouple is placed next to, but not touching, the outer diameter of the glass tube. In both tests, a copper wire is fed through the open end of the glass tube, down to the face of the copper plug. This allows dryout to be inhibited by preventing bubbles with the same diameter as the tube from forming. To start the test, the copper wire was retracted and video footage of the vapor was recorded.

The results of the test are compiled in Figs. 22 and 23. Frames were taken at second intervals from the first eight seconds after the wire was removed. Comparing the images, it can be seen that insulation causes dry out to occur much sooner, with the vapor bubble growing much larger. Additionally, the insulation reduced condensation and collapse of the vapor bubble. Although condensation was not eliminated completely, it was localized to the

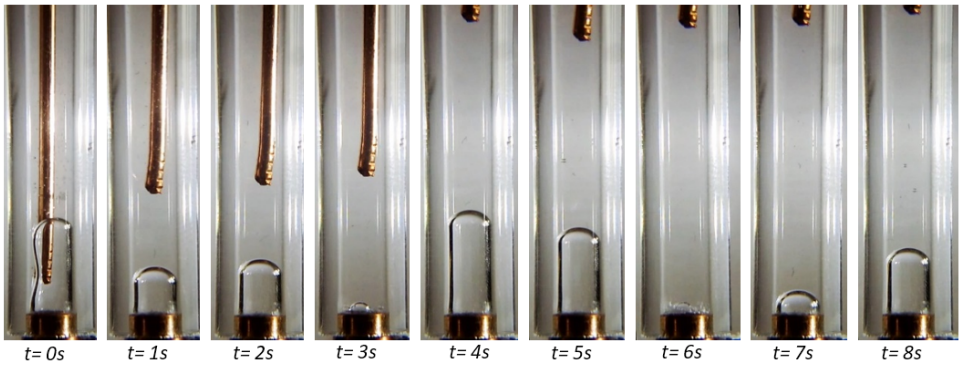

Figure 22: Dryout cycle without insulation

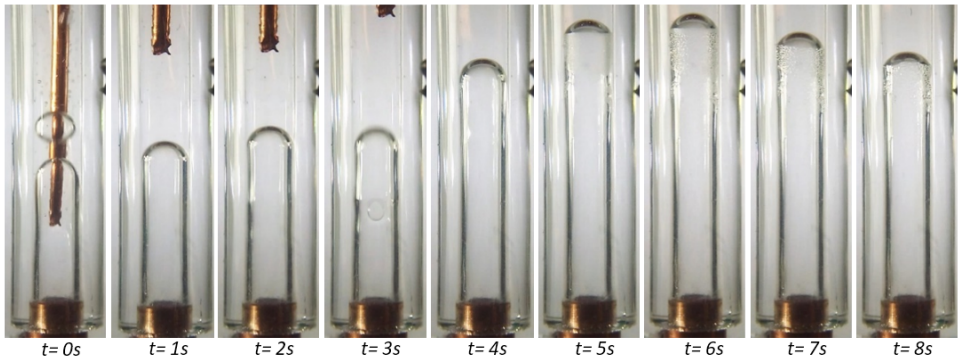

Figure 23: Dryout cycle with insulation

top of the bubble, as can be seen from five seconds on. Condensation on the inner diameter of the glass tube points to radial heat loss through the tube wall. Measurements of the air temperature next to the outer diameter also varied. As expected, the air trapped by insulation was heated to a higher temperature than in the trial without insulation. Interestingly, the air contained by the polycarbonate insulation experienced very slight temperature fluctuations around 50°C, while the temperature measurements in the other trial fluctuated between 22°C and 30°C with a period similar to that of the growth of the vapor bubble. From this, the decision was made to add an air-gap for insulation around the glass tube

to reduce transient behavior, and to better mimic the operation of a heat pipe by reducing heat transfer across the wall of the glass tube. Polycarbonate was chosen because of its high clarity and ease of machining, especially when compared to glass. The polycarbonate was specified to have an inner diameter of 0.5". This trapped a layer of air between the outer diameter of the glass tube and the inner diameter of the polycarbonate, whose thickness was below the critical thickness required for Rayleigh-Bernard convection cells to form. Initially, PLA end caps were printed to concentrically attach the polycarbonate to the glass tube. After these were observed to deform under heating, they were replaced with an ABS spacer at the cooling end, and the polycarbonate was extended to fit into the heating elements insulation. The extension of the polycarbonate into the heating element had the added benefit of directly heating the air in the gap, lowering the temperature gradient between the glass tube and the air, and inhibiting heat transfer. The ABS spacer was attached to the glass tube and the polycarbonate using silicone sealant. This is shown in Fig. 24, where a fully assembled experimental setup is shown, including the addition of thermocouples for plug temperature measurement.

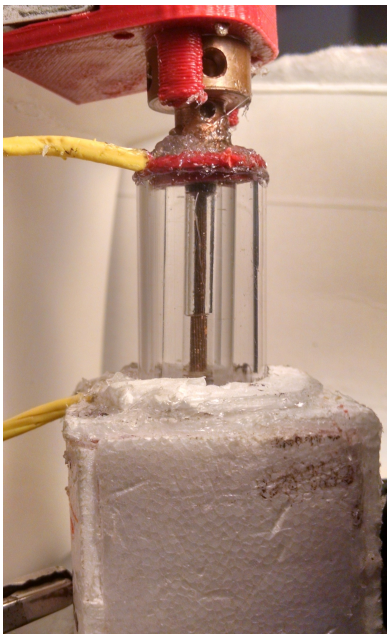

Figure 24: Fully assembled experimental setup.

Due to the wall thickness of the glass tube and the addition of a layer of polycarbonate, the effects of refraction became a concern, especially for potential measurement of distances from video images. In order to understand the amount of refraction taking place and its effects, a MATLAB code was written to provide a model. This code, attached in App. A, traces a light ray as it passes through the different media on its way to the wick. It then displays the traces of light rays, spaced at a user defined distance. The script uses Snells law[18] at each interface between different media. The code also allows for the surface normal to be plotted at each intersection. However, these are turned off in the finalized images. The X positions of each light ray's intersection with the working fluid to glass interface were recorded, and the spacing between them was compared to the original light ray spacing. The results are plotted in Fig. 25. Light ray traces from both working fluids are included in Fig. 26.

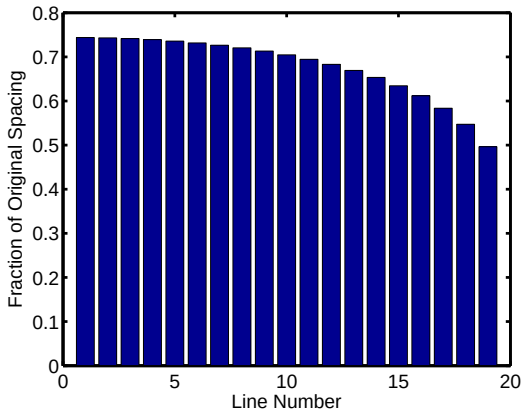

Figure 25: Difference in ray spacing at glass-working fluid interface.

2.3 EXPERIMENTAL PROCEDURE

This section discusses the experimental procedure carried out on the fully assembled experiment as shown in Fig. 24. The assembly procedure, including the method used to achieve

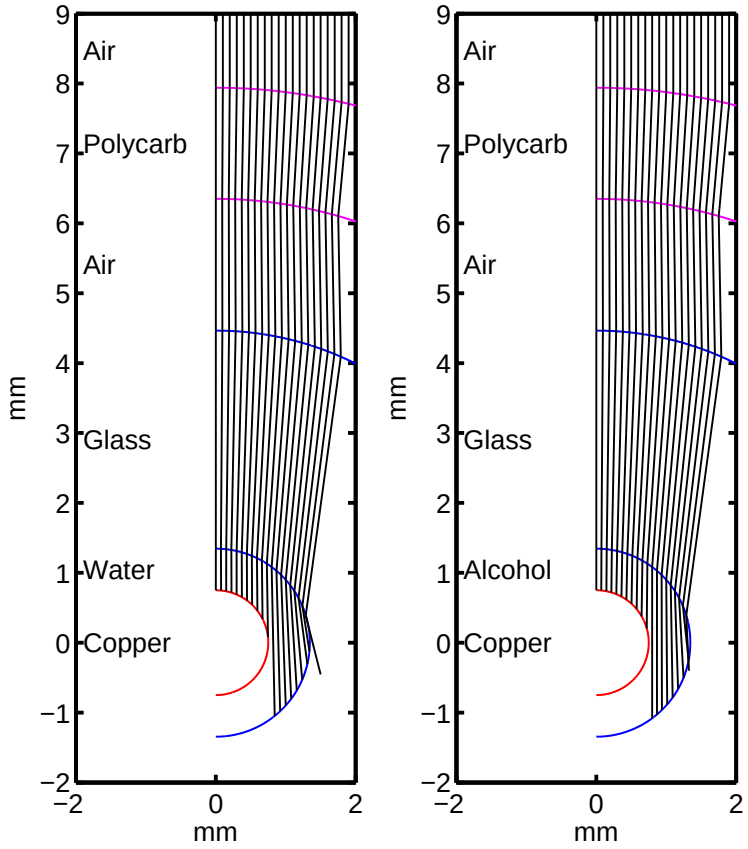

Figure 26: Light ray traces for water (left) and isopropyl alcohol (right).

different fill ratios, is outlined. Finally, the testing and measurement procedure used for each experimental trial is discussed.

2.3.1 Assembly and Set Up

First, all components in contact with the working fluid, including the plugs, wick, and glass tube, were cleaned. As mentioned previously, the assembly of these components will be referred to as the test section. The wick was treated with a vinegar-salt solution to remove any copper oxide build up on the wick surface. After being inspected for defects, O-rings

were fitted into the plug's machined grooves. The wick was then inserted into one of the plugs, and thermal paste was applied to the wick end to ensure good thermal contact between the wick and the plug. Silicone was then applied to the top face of the plug, both to prevent phase change on this face through insulation, and to cover any slightly shorter wires at the wick end. Silicone was applied in a similar manner to the other plug, with the end hole left uncovered to allow for wick insertion. The silicone was allowed to cure overnight. These components where then weighed on a Sartorius CPA324S Analytical Balance to establish a prefill weight. Following this, the plug and wick were inserted into one end of the glass tube, while submerged in the working fluid. After removal from the working fluid bath, the result was visually inspected for any air bubbles. Air bubbles were removed using a thin copper wire, and a syringe is used to ensure the glass tube was completely filled with the working fluid. Next, the plug and glass tube assembly was placed into the heating element. The other plug was lightly placed onto the opening of the glass tube. Power was applied to the heating element and the working fluid was heated until a two-phase mixture was achieved within the glass, preventing air leakage back into the volume. To prevent heat losses, a polycarbonate tube with a Styrofoam cap was used to confine the air surrounding the glass tube. Additionally, to prevent forced convection from air currents in the room, the heating was done under a clear covering. The partial filling procedure is pictured in Fig. 27.

Once a desired mixture of liquid and gaseous phases was achieved, the plug was fully inserted in the glass tube. In this way, the volume may be partially filled with the working fluid. The assembled test section was then weighed on the analytical balance, to allow for the mass of working fluid in the glass to be determined. After weighing, silicone was applied to the interface between the glass tube and the plugs to prevent accidental leakage through mishandling. Recorded weight data and calculated fill ratios are shown in table 3. The mass of the working fluid was found by subtracting the component's mass from that of the assembled test section. The working fluid mass was converted to volume using its density at room temperature: 998.2 kgm^{-3} for deionized water and 786 kgm^{-3} for isopropyl alcohol. This fluid volume is divided by an estimated test section volume, found using a solid model of the geometry. The assembled test section was now placed between the heating and cooling elements. Thermocouples were placed into the machined radial depressions in the plugs,

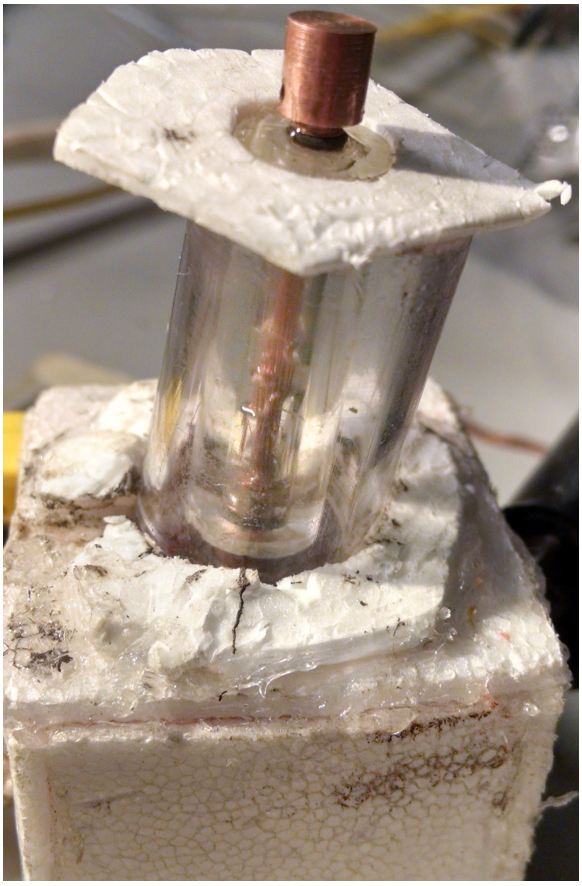

Figure 27: Partial filling of the test section.

with thermal paste in the depressions ensuring good thermal contact. Prior to assembly, the outside of the glass tube, and the polycarbonate were cleaned using isopropyl lens cleaning wipes. The polycarbonate was then slid into place, and its end cap fixed to both the top of the glass tube, and the polycarbonate with silicone. Finally, the vise was closed until the test section was seated firmly in the heating and cooling elements and the copper plugs. The vise places the test section in compression, securing the locations on the seals, and improving the thermal contact between the heating and cooling elements. Thermocouples were placed at the inlet and outlet of the cooling element. The fully assembled experimental setup is shown below in Fig. 28.

Table 3: Trial Fill Ratios

Trial	Component Mass (g)	Filled Mass (g)	Fluid Mass (g)	Fluid Volume (mm^3)	Percent Fill
Water 1	5.2598	5.2962	0.0364	36.4656	42.44
Water 2	5.2596	5.2855	0.0259	25.9467	30.20
Water 3	5.2559	5.2695	0.0136	13.6245	15.86
Alcohol 1	5.2562	5.2822	0.026	33.0788	38.50
Alcohol 2	5.2723	5.2943	0.022	27.9898	32.58
Alcohol 3	5.2777	5.2911	0.0134	17.0483	19.84

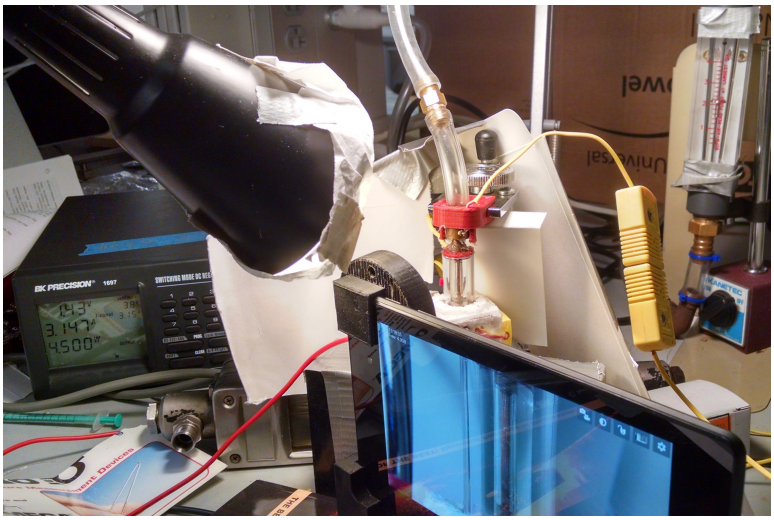

Figure 28: Assembled experimental setup.

2.3.2 Imaging

Video images were recorded by a Nexus 7 (2013) at a resolution of 1920x1080 and a framerate of 10fps. A magnifying lens was attached to the tablet using a custom printed PLA part. Prior to each trial, the lens was cleaned using isopropyl alcohol wipes. Images were captured

in the landscape orientation. Lighting was provided by a desk lamp with a thin paper covering to reduce glare, and the experiment was surrounded by white cardboard to provide a background with good contrast and to reflect light back towards the test section.

2.3.3 Temperature Measurement

Temperature was measured using K-type thermocouples welded from 1/16" wire. The potential difference across the thermocouples was read by a National Instruments Data Acquisition Unit 9211, and recorded using MATLAB. Samples were taken at a frequency of 1Hz, and plotted in real time.

2.3.4 Heating and Cooling Loads

Power was supplied to the heating element via a BK Precision 1698 DC power supply, set to constant current mode, to provide a stable, non-fluctuating supply wattage. Supplied wattage was displayed and could be adjusted easily through use of a knob. Alligator clips were used to attach to the wire ends of the heating element. Input wattage was recorded at the end of each trial, as the displayed wattage often changed because of temperature dependent resistance changes in the heating element. Heat was dissipated at the cooling element by compressed air. Air flow was measured in standard cubic feet per minute (SCFM) by a FL7311 rotameter from Omega. During an experiment, air flow was started prior to measurement and held at a constant rate throughout all trials. The rate of air flow was arbitrarily chosen to be 2 SCFM.

2.3.5 Experimental Trials

At the beginning of each trial, the video recording and temperature acquisition are started. While care was taken to make the beginning of the recording of the data sources as simultaneous as possible, both the processes were started manually. Video recording was started first, with temperature measurement beginning as soon as video recording was confirmed. The MATLAB script associated with temperature measurement required several seconds of

initialization, leading to a slight offset between the start of the two sets of data. Once logging of both data sources was visually confirmed, the power was adjusted to the first level. Data were recorded until the trial appeared to have reached steady state. This is measured by observing the change in temperature at each plug, over a span of two minutes. Once steady state was achieved, data collection was stopped. The video was downloaded from the tablet and the temperature data log file was saved. This usually took about 5-10 minutes. After the data was saved, the process is restarted, moving on to the next power level. Trials using deionized water as a working fluid were run first, followed by trials using 99% isopropyl alcohol. Power levels were increased by increments of one watt and increments of half of a watt, for water and alcohol respectively. The smaller increase in power input was used in the trials using isopropyl alcohol, to give a greater resolution on the effects on input power, and to gain insight into the performance below one Watt.

2.3.6 Uncertainty

Measurement uncertainty in the devices used during the experiments was briefly explored. The uncertainty of K-Type thermocouples as provided by manufacturer OMEGA was the greater of 2.2°C, or 0.75% of the measured value. Because of the range of temperatures measured in this investigation, the constant value was noted. The power supply had listed uncertainties of 0.2% and 0.5% in the supplied current and voltage, respectively. These combined for a 0.7% uncertainty in the supplied power. The resolution of the flow meter is 0.2 SCFM, which gives a measurement uncertainty of 0.1 SCFM.

3.0 DATA ANALYSIS

In this chapter, the steps taken to process the video images and the temperature data will the discussed. Additionally, the repeatability of the experiment will be evaluated.

3.1 VIDEO POSTPROCESSING

After recording the various trials described in Sect. 2.3, videos edited using Adobe Premier Pro. The test section was in a vertical orientation for all trials. However, video was recorded in a landscape, or horizontal orientation due to practical layout consideration and, because of this the majority of each frame contained images not relevant to this investigation. Therefore, the primary objective of editing was to crop each frame so that only the test section was present. The cropped video files had resolutions of 160-200x920-1060, depending on the position of the camera. This considerably reduced the video file size and made it easier to focus on the phenomena occurring inside the test section during playback. Additionally, videos were straightened and the audio channel was removed from each file. Further video postprocessing was done using a MATLAB script included in App. B. This script took one frame each second from the video file, and overlaid a time stamp and the temperature data record onto the frame at appropriate locations. The processed frames were then compiled into a new video file with a frame rate of two frames per second, or double the original recording speed. Extra care was taken during MATLAB processing to ensure that the resolution of each frame was preserved. The resulting video files allowed video and temperature data to be viewed simultaneously, since it was hoped that this would help further analysis. The MATLAB processed video files were also much smaller than the originals, while preserving

many of the phenomena of interest. Often, the abridged MATLAB processed video files were used to gain a general overview of behavior, and the original full frame rate files were used to observe specific phenomena noted in the MATLAB processed video files. Frames from the beginning and end of each trial were taken and compiled into figures by fill ratio. This allowed the effect of input power to be visually seen for each fill ratio.

3.2 DATA PROCESSING

Following the temperature data acquisition, the condenser temperature was subtracted from the evaporator temperature to find the temperature difference across the test section. This temperature difference across the heat pipe was plotted against the trial time data, and the mean of the steady state portion of this curve was recorded. This was repeated for each trial. The averaged steady state temperature of each trial was used to find the thermal resistance, as shown in eqn. 1.1, and plotted for each fill ratio and working fluid combination. To determine the time rate of change of the temperature at both the condenser and the evaporator, the difference between data points a fixed time difference apart was calculated and then plotted against time. A fifth-order trend line was fitted to the time rate of change data, and the average absolute difference between the data points and the trend line was recorded for each trial. The time rate of change data was also filtered to make it easier to see deviations not caused by thermocouple noise. Temperature data from the cooling element was analyzed to determine the increase in temperature across the cooling element. This measured temperature increase was compared to an expected temperature rise. The expected temperature rise, assuming steady state and that all energy input at the heating element is dissipated at the cooling element, is calculated by eqn. 3.1:

$$\Delta T_{rise} = \frac{\dot{q}}{\dot{m} C_p} \tag{3.1}$$

where ΔT_{rise} is the expected temperature rise, $\dot{q}$ is the input power, $\dot{m}$ is the mass flow rate of the cooling air, and C_p is the specific heat capacity of the cooling air. Assuming conditions in the lab are reasonably close to STP, the specific heat capacity of air is 1.006 kJ(kgK)$^{-1}$,

and SCFM can be converted to cubic feet per minute (CFM). Using the density of air at STP, a mass flow rate of 944 cm^3s^{-1} can be calculated. Since the cooling air flow rate was kept constant, using egn. 3.1, the expected temperature rise of the cooling air flow can be calculated as a function of input power.

3.3 EXPERIMENTAL REPEATABILITY

Experimental repeatability was analyzed by running four 'dry' tests. A 'dry' trial run is a run conducted without any working fluid in the test section. Although air was still present in the test section, it was assumed that the circulation of this air would not contribute significantly to heat transfer across the test section, because of its low heat capacity per unit volume, and its inability to change phases. The dry configuration was chosen because of the difficulty of filling the test section to a precise level. Temperature data for both of these runs were compared to each other, in an attempt to analyze the effect of the minute differences in setup between different trials. The one trend line was created from the data sets and then the confidence interval that bounded the points was found. The goal of this analysis was to show that the measurement and test section conduction effects between trials were almost constant. The results of each trial, along with a confidence interval and average, are plotted in Fig. 29. The MATLAB code used to do this analysis is included in App. C. The maximum confidence interval offset from the trendline was 1.76°C, below the thermocouple uncertainty noted in Sect. 2.3.6. Differences between trials could be explained by differences in ambient conditions, due to the lab's HVAC system, and the integrity of thermal contact between components.

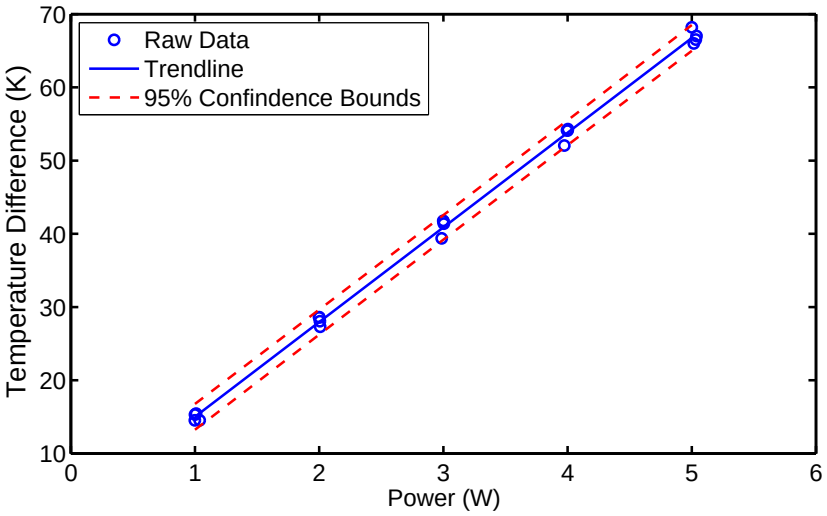

Figure 29: Experimental repeatibility tests with trendline and 95% confidence bounds.

4.0 RESULTS

In this chapter, the results of testing and data analysis will be presented and discussed. First, a qualitative analysis of the video recordings, along with still images, will be presented. Following this, the results of data analysis performed on acquired temperature data will be discussed. Finally, an attempt will be made to make connections between the two different types of data that were collected.

4.1 QUALITATIVE DISCUSSION OF VIDEO IMAGES FOR WATER TESTS

In this section, the general behavior observed in the recorded video will be discussed. The overall phase distribution for each trial will be shown, in addition to specific phenomena. The differences between fill ratios for water trials will be discussed.

4.1.1 Water at a 15% Fill Ratio

In the video recordings, before heat was applied to the test section with water at a 15% fill ratio, the liquid phase had formed a droplet contained between the wick and glass tube as can be seen in Fig. 30. After applying one Watt of power, the liquid phase was mainly condensed on the inner surface of the glass tube, and the beginnings of a dry out effect could be seen at the base of the tube. Condensation droplets formed slowly and did not coalesce quickly. The largest condensation droplets spanned between the glass tube wall and the wick, but did not wrap around to create plugs. Once these droplets had reached a critical

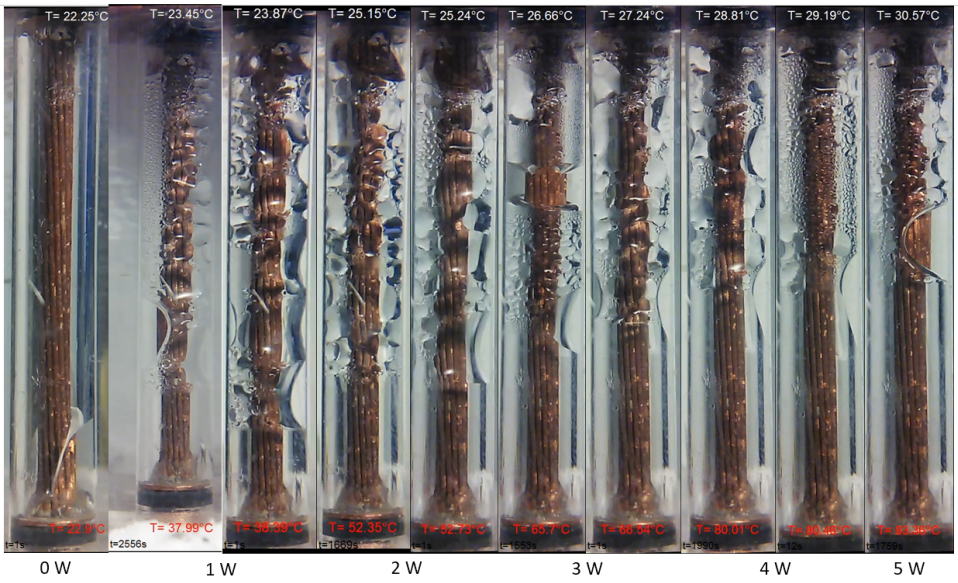

Figure 30: Stills from video for water at a 15% fill ratio.

size, they traveled down the test section, coalescing with smaller droplets as they went. The time required for a droplet to move this distance is on the order of seconds.

Liquid condensing at the top of the tube spanned the entire heat pipe cross section. The amount of condensed liquid in the condenser increased when there was liquid in the evaporator and shrank when the evaporator section was dry. The liquid from the condenser was not observed to travel down the test section to the evaporator. Evaporator rewetting occurred primarily by the mechanism of droplets coalescing on the inner diameter of the glass tube, until a critical mass was reached. Once the critical mass was achieved, droplets slid down the glass surface, coalescing with smaller droplets below them. Droplet motion stopped when a plug of liquid was formed, or when the droplet reached the dried out portion of the test section. In both cases, droplet motion appeared to be affected strongly by surface tension forces. As the input power was increased, the size of the dried out region increased until it occupied about half of the tube volume at five Watts, as seen in Fig. 30. The size of the droplets on the tube wall also increased as the input power was increased, due to the change in vapor deposition rate, and the larger dried out surface area.

4.1.2 Water at a 30% Fill Ratio

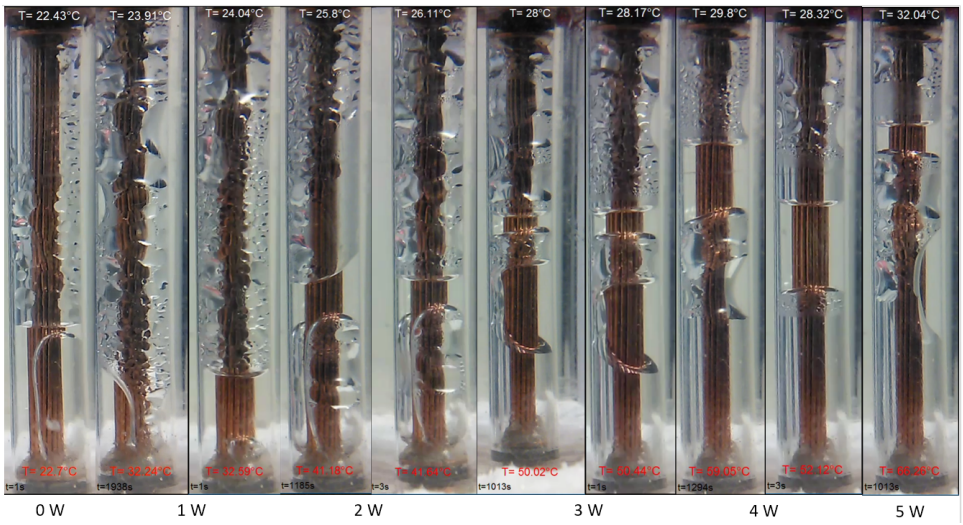

Figure 31: Stills from video for water at a 30% fill ratio.

For a 30% fill ratio, before power was applied, the bottom of the test section was filled with liquid. A large vapor bubble was present within this liquid as can be seen in Fig. 31, held in place by surface tension forces. The portion of the test section occupied by vapor had large droplets occupying the inner surface of the glass. After one Watt of power was applied to the test section for approximately 60 seconds, the vapor bubble at the base coalesced with the vapor above it; however, the space occupied by it was not immediately rewetted. Areas of the inner surface of the glass tube that had not been previously occupied by liquid droplets were now covered in a fine mist. The rewetting of the evaporator occurred over the next several minutes, with the liquid-vapor interface advancing slowly as the liquid coalesced with droplets on the tube's inner diameter. Once the liquid-vapor interface at the evaporator reached a critical point, the liquid flowed rapidly to encompass the wick and fill the bottom of the test section. As the input power was increased, vapor bubbles grew in the liquid filling the evaporator. At low power levels, these bubbles grew until they reached the liquid-vapor interface above the condenser. Oddly, they did not coalesce and completely encircle the wick. This process was often inhibited by liquid droplets which moved to the evaporator and raised the liquid-vapor interface.

When the input power was raised to three Watts, the vapor bubbles coalesced to completely encircle the wick. The vapor bubbles in the evaporator continued to grow until reaching the liquid-vapor interface. For a moment, the volume closest to the wick was occupied by vapor, while the liquid was present primarily in droplets on the glass surface, with a small droplet present at the bottom of the test section. The liquid on the glass surface then rapidly coalesced and filled the evaporator. In the evaporator, a portion of this liquid quickly flashed to vapor. However, the vapor generated in the evaporator was prevented from traveling to the condenser by a plug of liquid, which was pushed ahead of the vapor bubble as it grew. Following this, the evaporator slowly dried out, with rewetting being prevented by the vapor bubble. As the power level was increased, similar behavior to that observed for water at a 15% fill ratio occurred; however, the test section was effectively split by the water plug above the evaporator. Following the increase of input power to four Watts, the same phenomena described when the power was increased from two to three Watts occurred, only higher up the test section due to evaporator dry out. This behavior was not observed again. When compared to trials with water at a 15% fill ratio, the volume of liquid accumulating around the wick in the condenser was small.

4.1.3 Water at a 40% Fill Ratio

At low power levels, the test section with water at a 40% fill ratio, as seen in Fig. 32, behaved similarly to the 30% fill ratio testing discussed in the previous section. It is important to note that the second trial in Fig. 32 (the third frame from the left), was started at zero watts of power. At low power levels, two vapor bubbles formed independently of each other on opposite sides of the wick and grew, moving toward the liquid-vapor interface. As previously mentioned, the interface shifted upwards because of rewetting flow down the glass surface. At two Watts of input power, when these vapor bubbles reached the interface, they stretched and tore at the middle. The top portion of the bubble traveled across the interface, while the bottom portion remained in the evaporator and continued growing. When the input power was increased to three Watts and the vapor bubble again reached the interface, the same phenomena described for a 30% fill occurred, and a liquid plug formed. The liquid plug for a

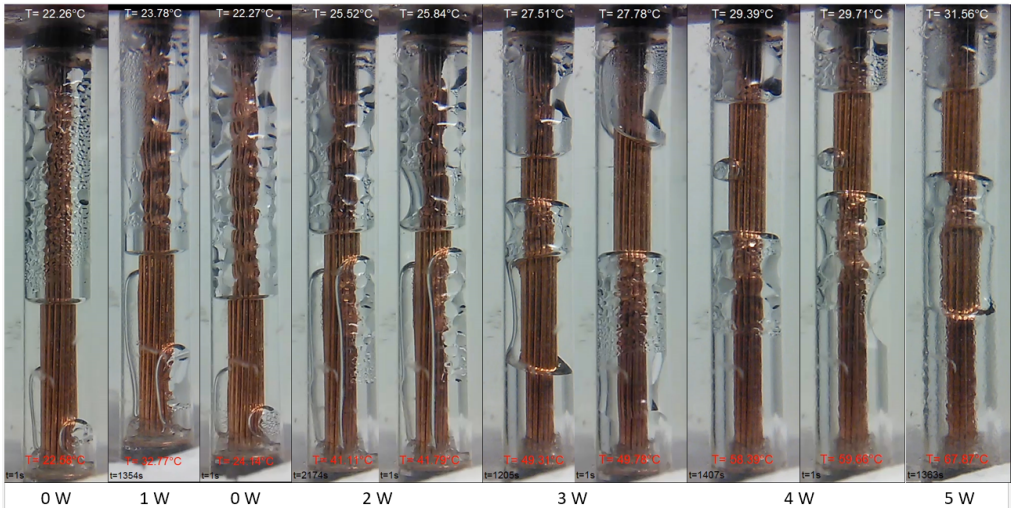

Figure 32: Stills from video for water at a 40% fill ratio.

40% fill ratio was much larger, due to the higher fill ratio. Liquid was present much further down the test section at higher power levels, when compared to the 15% fill and 30% fill. A behavior similar to plug formation occurred when the power was increased to four Watts; however; in this case the original plug was still intact. Instead of a new plug forming, the size of the original was increased. The volume of liquid present in the condenser was small across all power levels, similar to the 30% fill ratio. As with the other fill ratios, as the input power was increased, the portion of test section that was dried out grew.

4.1.4 Comparing Water Fill Ratios

For all trials, as the fill ratio of the test section was increased, the size of the dried out region decreased, especially at higher power levels. This can be clearly seen when comparing the 15% fill trial in Fig. 30 to the 40% trial in Fig. 32. Additionally, trials with higher fill ratios showed the formation of liquid plugs separating the vapor in the test section. A small plug only briefly formed during the 15% fill ratio trial, as shown in Fig. 30 (the sixth frame from the left), while large plugs are present throughout the 30% and 40% fill tests. As the fill ratio increased, the size of these plugs was also seen to increase. Only at the lowest fill ratio

was a sizable volume of liquid visible in the condenser of the test section. Generally, fluid circulation within the heat pipe occurred slowly for all water trials.

4.2 QUALITATIVE DISCUSSION OF VIDEO IMAGES FOR ISOPROPYL ALCOHOL TESTS

In this section, the observations of the video recorded for alcohol trials will be discussed. Overall phase distribution by power level will be shown, in addition to behaviors specific to alcohol as a working fluid.

4.2.1 Alcohol at 20% Fill Ratio

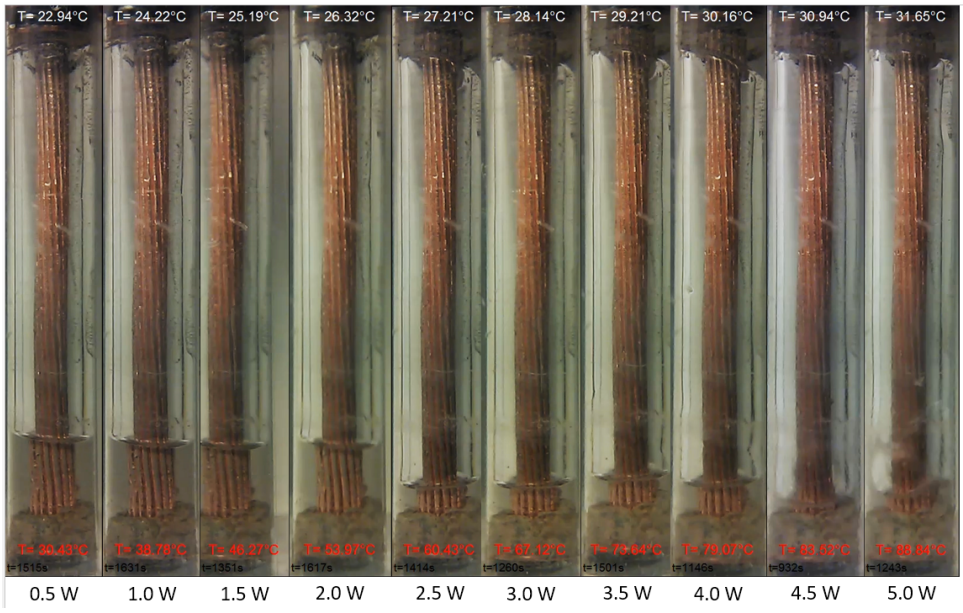

Figure 33: Stills from video for alcohol at a 20% fill ratio.

When a heat load was first applied to the test section that was 20% filled with isopropyl alcohol, as shown in Fig. 33, the liquid level in the evaporator dipped slightly. This was paired with the presence of liquid in the condenser. As the power level was increased, the

evaporator liquid level continued to lower slightly. Liquid as a film became visible on the glass surface. Overall, fluid circulation and phase change were difficult to observe at lower power levels. Once the input power was increased to two and a half Watts, the liquid level in the evaporator dropped sharply, while the volume of liquid present in the condenser increased. This continued until the liquid in the condenser reached a critical volume and flowed down the test section to the evaporator. Condenser liquid build-up followed by evaporator rewetting formed a repeating cycle. As the input power was increased, the period of the cycle also increased. At the beginning of each trial, the period of the rewetting cycle decreased rapidly, until it reached an equilibrium value. The time between rewetting events was recorded and is presented in Fig. 34.

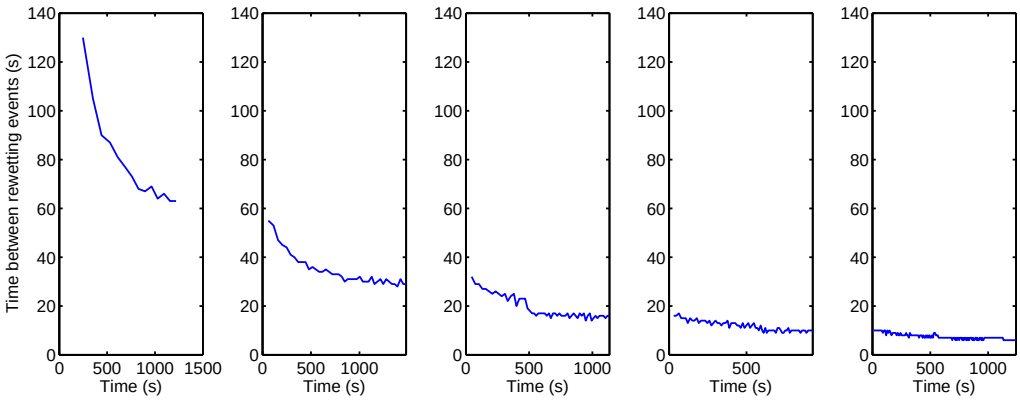

Figure 34: Time between rewetting events for input powers of 3, 3.5, 4, 4.5, and 5 W from left to right.

When the power input was increased to four Watts, violent phase change, similar to nucleate boiling, was observed in the liquid in the evaporator. As the power level increased further, this phase change became increasingly violent and chaotic. Despite this, the evaporator was never observed to be completely dried out.

4.2.2 Alcohol at 32% Fill Ratio

The alcohol trial with a 32% fill ratio began similarly to the 20% fill ratio, as can be seen in Fig. 35. Upon heat load application, there was a slight dip in the liquid level in the

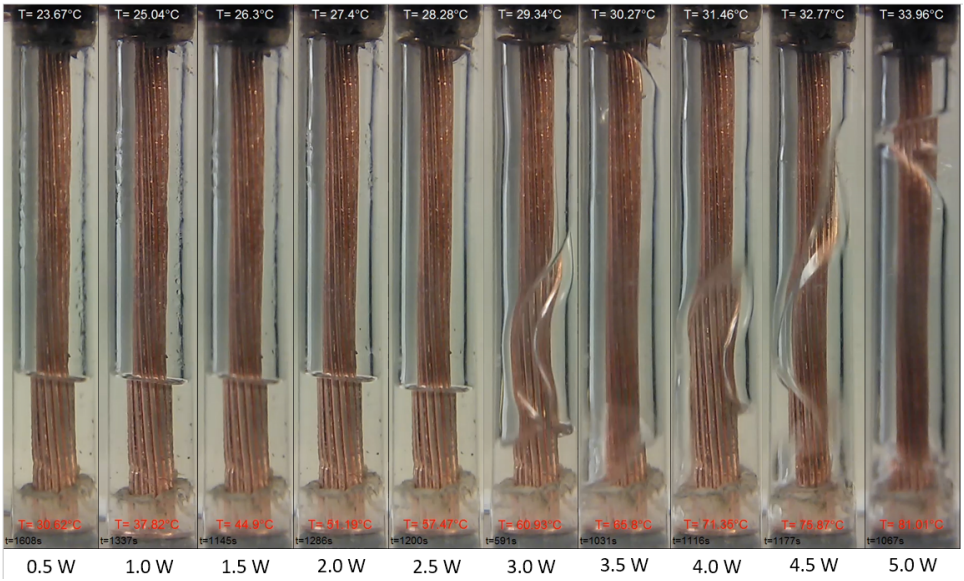

Figure 35: Stills from video for alcohol at a 32% fill ratio.

evaporator, and soon after, condensed liquid could be observed in the condenser of the test section. Liquid alcohol could clearly be seen condensing on the surface of the glass. This was not observed in the trial with a 20% fill ratio. As with the 20% fill ratio, visible fluid circulation did not occur until higher input power levels were achieved. The first observable instance of fluid moving from the condenser to the evaporator occurred at the end of the trial with an input power of two and a half Watts. After this first circulation event, events presented more frequently, much like in the 20% trial. However, discrete circulation events were much more difficult to observe than with a 20% fill ratio, because of a chaotic liquid-vapor mixture present throughout the test section, as shown in Fig. 36. As can be seen from the time stamps included in Fig. 36, this behavior happened rapidly, too quickly to capture accurately at the low frame rate used.

While it was possible to observe certain events, often liquid in the condenser would reach a critical volume not because of the condensation of vapor, but because it coalesced with liquid that had been propelled up the test section from the evaporator. Even though it was difficult to observe these events, it was clear that their frequency increased with input

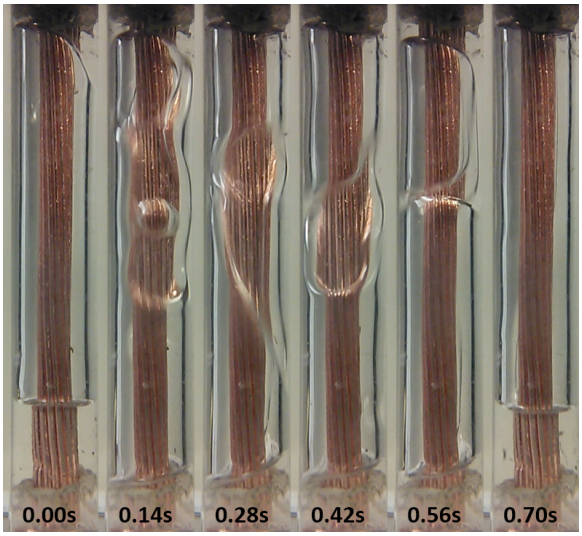

Figure 36: Chaotic phase distribution for alcohol 32% fill at 3 Watts.

power. Additionally, as the input power was increased, less and less liquid was present in the evaporator and condenser. The majority of the liquid appeared to be in a thick film on the inner surface of the glass. The movement of fluid within the test section also became much more violent and chaotic as the input power was increased.

4.2.3 Alcohol at 39% Fill Ratio

The experimental trial with alcohol at a 39% fill ratio also began similarly to the other alcohol trials, as shown in Fig. 37. When power was first applied, a small amount of the liquid phase moved from the evaporator to the condenser. However, in contrast to trials with other fill ratios, visible phase change in the evaporator occurred much more rapidly. At one watt of input power, vapor bubbles formed inside the liquid in the evaporator. It was difficult to tell whether these vapor bubbles crossed the liquid-vapor interface and traveled to the condenser, or collapsed in the liquid present in the evaporator. However, the lack of liquid build up in the condenser suggested the former. As the power input was increased, these vapor bubbles could be seen to clearly cross the interface, causing a phase distribution similar

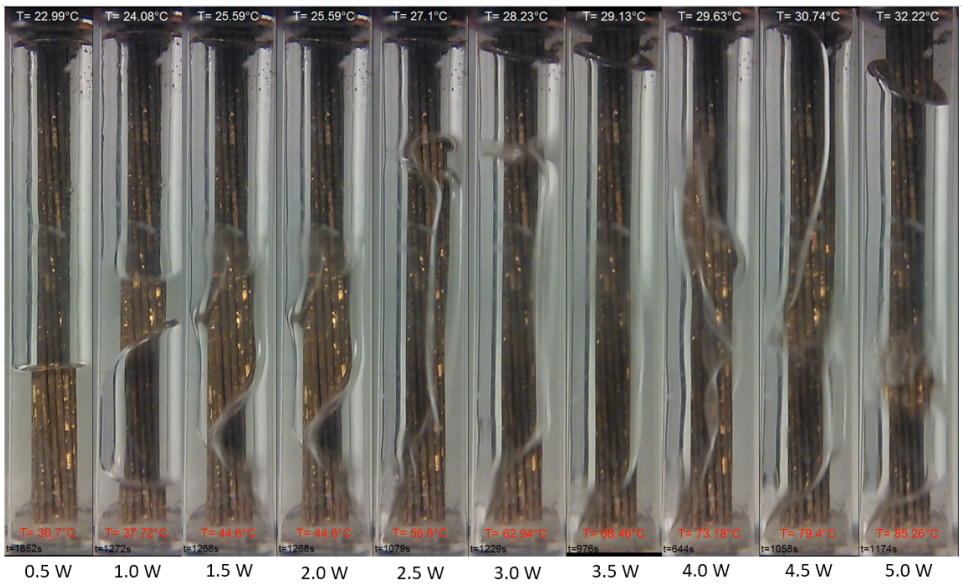

Figure 37: Stills from video for alcohol at a 39% fill ratio.

to that seen in Fig. 36. Additionally, the beginnings of liquid buildup in the condenser could be observed. However, no rewetting events were noted, beyond film flow on the glass surface. Following an input power increase to two Watts, the phase change in the evaporator became violent enough that liquid was forced up to the condenser. This caused the liquid that had built up in the condenser to return to the evaporator. As with the other trials, the fluid behavior in the test section became increasingly violent and chaotic with increasing input power. When compared to the other alcohol fill ratios, the volume of liquid that accumulated in the condenser before returning to the evaporator was much larger.

4.2.4 Comparing Alcohol Fill Ratios

All alcohol trials showed liquid buildup in the condenser and a rewetting flow of condensed liquid to the evaporator. This rewetting flow took the form of a large droplet, as the power and therefore the rate of vapor generation increased. This rewetting flow showed a periodic behavior, which decreased in time as the applied power was increased. Fig. 34 clearly shows

the decrease in time between rewetting flow events, and while discrete events were difficult to document for the higher fill ratios, the same increase in frequency with power could be qualitatively seen. In all trials, a liquid film could be seen on the inside of the glass tube. The film thickness appeared to remain largely constant, except for the 32% fill ratio, where increasingly chaotic behavior led to a thickening of this film. Although all fill ratios showed violent phase change in the evaporator and a chaotic fluid distribution, the power level at which these behaviors were first noted varied. For the 39% fill ratio these began almost immediately, as soon as the power was increased to one watt. For the 32% fill ratio, this point occurred at three Watts. Finally, the 20% fill ratio did not show rewetting events until two and a half Watts of applied power, and violent evaporator phase change until four and a half Watts of input power.

4.3 COMPARING ALCOHOL AND WATER AS WORKING FLUIDS

Fluid circulation occurred much more rapidly for trials using alcohol as a working fluid, when compared to those using water. None of the violent, rapid phase change seen in alcohol trials, and shown in Fig. 36, was seen in any of the water trials. A major difference between fluid distribution between the two working fluids was the liquid phase on the inner diameter of the glass tube. For the alcohol, the liquid coated the glass surface in a film. This film allowed liquid to move easily from the condenser to the evaporator, in addition to insulating the vapor in the center. In contrast, water condensed on the glass surface in droplets that grew in size. Once these droplets reached a critical size, they slid down the glass surface to the evaporator. As the droplets moved towards the evaporator, they coalesced with the droplets below them, clearing the surface for new condensation.

Alcohol was unable to form plugs that completely filled the cross section between the wick and the glass surface, like those seen for trials with water. These liquid plugs divided the heat pipe and prevented vapor formed in the evaporator from traveling to the condenser. Likewise, condensed liquid was prevented from traveling to the evaporator, and instead coalesced with the plug. Additionally, the liquid plugs were generally far from the evaporator,

which inhibited their phase change to vapor and effectively removed the liquid they contained from the heat pipe.

None of the trials using alcohol as a working fluid had complete evaporator dryout, even at the highest power levels. While all fill ratios of water showed some level of dryout as the input power was increased. Preventing evaporator dryout is important, because as was mentioned in Sect. 1.2, dryout adds an additional thermal resistance to the heat pipe. Under dryout conditions, heat energy must be conducted through a portion of the length of the test section, adding a temperature drop and increasing thermal resistance.

The differences in working fluid motion and phase distribution can be attributed to the material properties of the working fluids that were studied. Water's higher surface tension caused it to bead up on the tube wall and form plugs across the test section, while alcohol's low surface tension allowed for more rapid fluid motion through the test section.

4.4 TEMPERATURE DATA ANALYSIS

In this section, the results of the data analysis described in Sect. 3.2 will be presented. Conclusions about the thermal performance of the different trials tested will also be discussed.

4.4.1 Heat Losses Across the Test Section

The results of the temperature rise for selected trials can be seen above in Fig. 38. Also shown on this plot are the calculated cooling air temperature increases for different percentages of heat loss across the test section. Appreciable losses can be seen for all trials, especially at high power levels. Potential areas for heat loss were the heating element insulation, radially across the wall of the borosciliate tube, and conduction between the cooling element and the cooling element holder. Interestingly, alcohol trials perform much better than water trials, especially at low power. This could be due the thin liquid film that could be seen on the inner diameter of the glass tube at low input powers. This film could have insulated the test section, and ensured that phase change, and therefore heat transfer, occurred at the

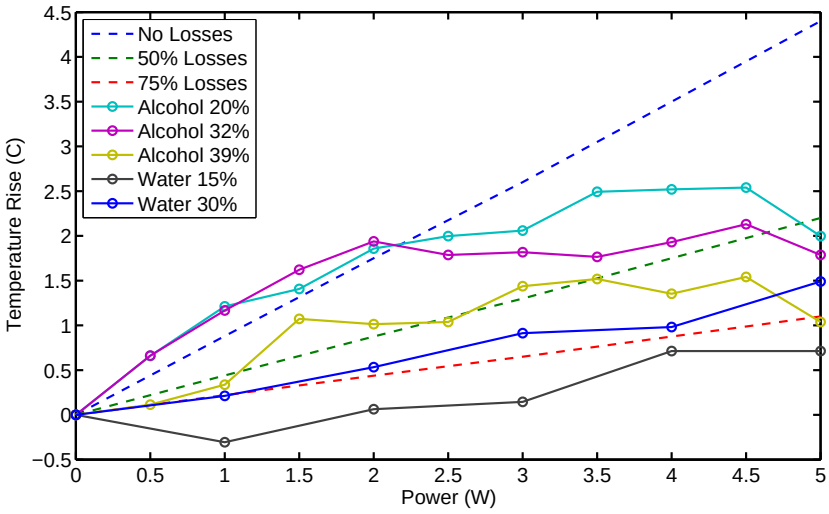

Figure 38: Temperature rise in cooling air.

condenser. As the input power was increased, this film was disrupted and this could have reduced its insulating effects. The high heat losses for water trials could have been due to vapor condensation on the glass surface. When vapor condensed on the surface of the glass tube, its thermal energy was deposited there and not in the condenser. This energy may have been lost radially from the surface of the glass tube, despite insulation attempts.

4.4.2 Thermal Resistance Across the Test Section

The thermal resistance for each trial was calculated using eq. 1.1, with the temperature difference across the test section recorded at steady state. The results are plotted in Fig. 39. Analyzing the effect of fill ratio on thermal resistance, there appeared to be an optimal fill ratio as suggested by the literature. Of the trials conducted for both working fluids, a fill ratio of 30% appeared to be optimal. Interestingly, there was little difference between a 30% fill and a 40% fill for water trials. The alcohol trials, on the other hand, showed a thermal resistance increase past the optimal fill ratio. The alcohol trials were grouped closely together when compared to the difference between water at 15% and the other water trials.

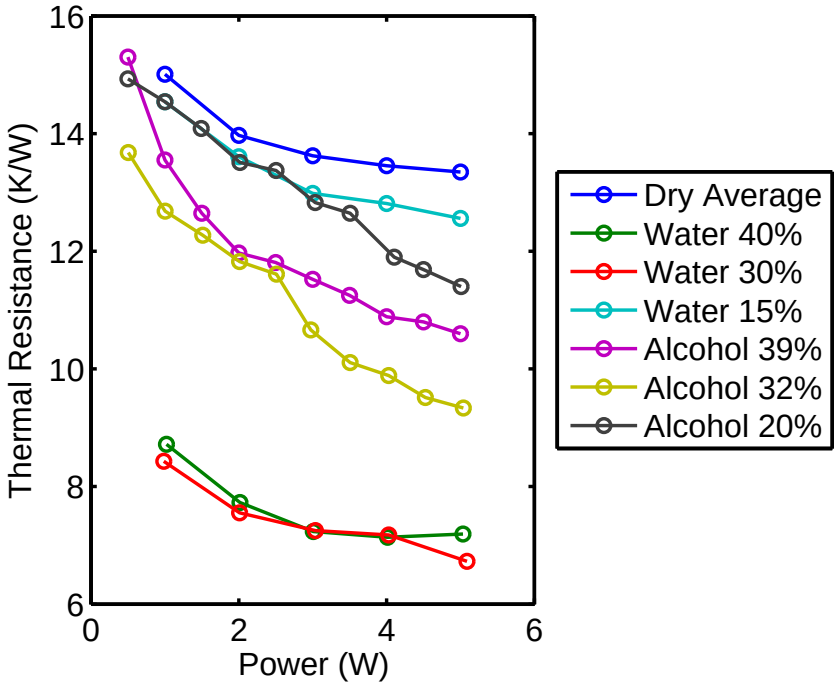

Figure 39: Thermal resistance across the test section plotted by input power.

Although water appeared to have superior performance as a working fluid when compared to alcohol, the trial with water at a 15% had the highest thermal resistance. Its thermal resistance was higher than even the lowest alcohol fill ratio, especially as the input power was increased. The thermal resistance results for both working fluids suggests that alcohol's greater mobility through the test section was less important than water's much higher latent heat of vaporization.

For all trials, the thermal resistance decreased as the input power was increased, especially at lower power levels. This decrease was most dramatic for the trials using alcohol as a working fluid. This decrease was also seen in the literature and is attributed to the start up of heat pipe operation. Interestingly, two of the alcohol trials showed a second drop in thermal resistance. This drop occurred between 2.5 and 3 Watts for alcohol at 32% and between 3.5 and 4 Watts for alcohol at 20%. The drop for the 32% alcohol trial coincided

with the beginning of fluid circulation, as seen in Fig. 35. The thermal resistance drop for the 20% trial coincides with the appearance of increasingly violent phase change in the evaporator.

4.4.3 Distance from Trendline

As the input power was increased, increasingly rapid and violent fluid motion was noted in all experimental trials. In order to see if this was represented in the temperature data, the analysis described in Sect. 3.2 was performed. In Figs. 40 and 41, the average difference is shown between the treadline and the time rate of change data calculated for both the condenser and the evaporator is shown. These are plotted by trial number, with the power increasing to five Watts for the last trial.

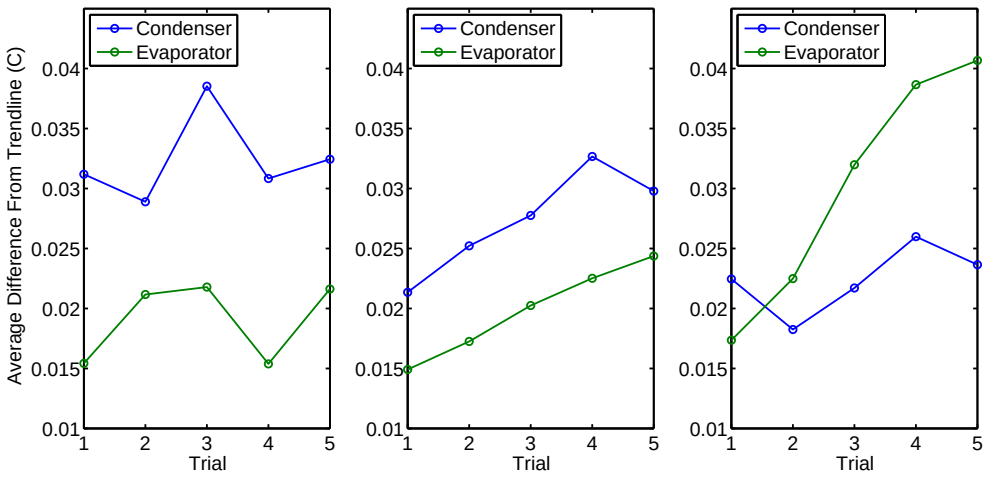

Figure 40: Average difference from the trendline for water at 15%, 30% and 40% fill ratios, from left to right.

The water trials in general showed that as the input power was increased, the average difference between points on the trendline increased. Interestingly, data from the lowest fill ratio for water did not display an upward or downward trend. Trials using alcohol as a working fluid showed a much clearer positive trend between the difference from the trendline and the input power. For alcohol, higher fill ratios appeared to show a more positive trend.

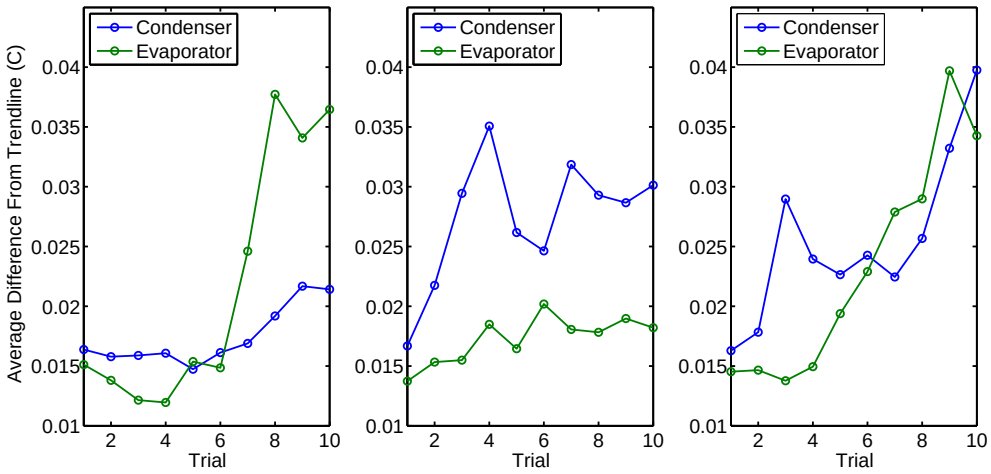

Figure 41: Average difference from the trendline for alcohol 20%, 32% and 39% fill ratios, from left to right.

This was consistent with observations of the video images recorded, where fluid motion was most violent at the highest fill ratios. Early spikes in the condenser curves for the higher alcohol fill ratios could have been caused by the beginnings of fluid droplet flow from the condenser to the evaporator.

4.5 RELATIONSHIP BETWEEN VIDEO AND TEMPERATURE DATA

Observations of peaks in the time rate of change curves for the evaporator and the condenser raised questions about the events that caused these peaks, and if they had been recorded in the video footage. These curves generally followed a decaying trend, as the trial approached steady state. However, deviations from this trend could be seen in nearly all of the trials. When observing video images, these deviations could be seen to be caused by the movement of phases. For evaporator temperatures, spikes upwards coincided with evaporator dryout, following vapor generation. Conversely, dips form the trend point to rewetting of the evap-

orator by the liquid phase. Some of these events are difficult to visualize, as video was only taken from one angle and only half of the test section was visible. An example time rate of change curve from the evaporator for water at a 15% fill ratio is shown in Fig. 42. Clear deviations from the trendline can be seen at 391, 596, 1036, 1096 and 1356 seconds. The

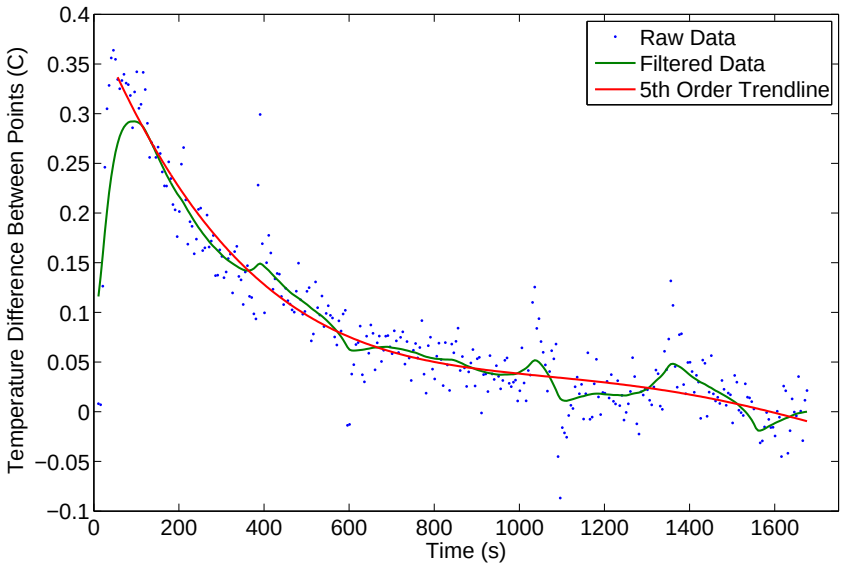

Figure 42: Time rate of change curve for evaporator for water at 15% fill ratio at 2 Watts.

frames surrounding the dip at 1096 seconds and the peak at 1356 seconds are shown in Fig. 43. The video time stamps are slightly offset from those of the temperature data, because of the difficulty of simultaneously starting both video recording and temperature measurement, mentioned in Sect. 2.3.5. As the frames on the left of Fig. 43 show, a liquid droplet traveled down the test section and coalesced with liquid already present at the evaporator end. Liquid water now completely surrounded the evaporating section of the test section. The presence of the liquid phase lowered the evaporator temperature rise, because of the heat energy required for phase change. The frames on the right of Fig. 43 show a liquid droplet evaporating on the surface of the wick. In the final frame the evaporator section of the wick was completely dry. Energy that was previously being used to change the phase of the liquid droplet now caused a temperature rise in the evaporator.

Unfortunately, it was difficult to find similar comparisons between temperature data and

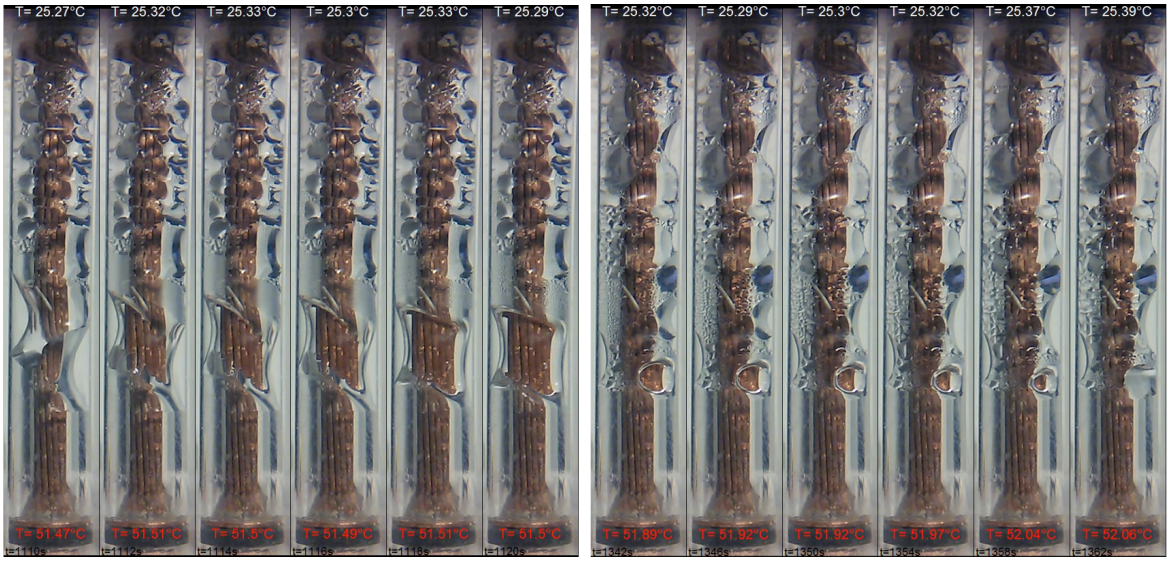

Figure 43: Evaporator rewetting (left) and dryout (right) for water at 15% fill ratio at 2 Watts.

video recordings when alcohol was used as a working fluid. The significantly more rapid fluid motion between the evaporator and condenser in the alcohol trials may have been impossible to capture at the relatively low sampling frequency used for data collection. In the alcohol trials, dryout and rewetting events occurred more frequently than in the water trials, which could lead to many small deviations, instead of the few, large deviations seen in Fig. 42 and other water trials. Alcohol also has a much lower latent heat of vaporization than water, see table 1, which could also contribute to reducing the magnitude of these deviations.

5.0 CONCLUSIONS

The observations of the recorded video showed that the working fluids chosen for this investigation behaved very differently. In the alcohol trials, fluid circulated easily between the condenser and the evaporator. While in trials using water as a working fluid, fluid motion appeared almost stagnant in comparison. However, trials using water as a working fluid showed much lower thermal resistance. For both working fluids, evidence of an optimal fill ratio of around 30% of the total volume was seen in the thermal resistance plots.

The experimental setup used in this investigation performed largely as expected. However, large heat losses and the presence of condensation and fluid flow on the inner surface of the glass tube are concerns, because they indicate that some of the assumptions made in Sect. 2.1 are not valid. The boundary represented by the inner surface of the glass tube was assumed to be adiabatic and free of liquid. The presence of liquid on this surface also obscured any observation of fluid flow or phase change on the wick face.

A major success of this investigation were the links found between temperature data and video images. Phase distribution and movement may be predicted through temperature measurements at different locations. These measurements must be accurate and frequent enough to capture the working fluid. The accuracy and frequency of temperature measurements should be informed by the working fluid material properties. This investigator suggests using the latent heat of vaporization and the surface tension, respectively.

5.1 RECOMMENDATIONS FOR FUTURE WORK

Future investigations recording temperature data and video data should use a higher sampling frequency than the one used in the present investigation. This especially true when the working fluid has a low surface tension and low latent heat of vaporization, such as isopropyl alcohol.

In order to fully capture the test section, future investigations should use two cameras from different angles. Also, temperature data and images should be recorded by the same devices so that there is no time offset between the two data sources.

The insulation of the outer diameter of the glass tube should be improved as well. Currently, a passive air-gap insulation is used, but a solution using a heat load to actively cancel the measured heat flux across this surface may yield better results.

Further testing is recommended to expand on the connection between observations of working fluid flow and temperature measurement. Through the use of fine enough temperature measurements, it may be possible to analyze fluid behavior in a heat pipe with greater accuracy.

APPENDIX A

MATLAB CODE USED TO CALCULATE REFRACTION

```
clc
close all
clear all
set(0,'defaultLineLineWidth', 1)
for ak=1:2
    nair=1.0003;
    %nwater=1.3330; %nalcohol=1.3772;
    nfluid=[1.3330 1.3772]; nglass=1.525; npoly=1.585;
    fluid=['Water  ';'Alcohol'];
    fluid=cellstr(fluid);
    x=0:0.1:2;
    %Geometry
    theta=-pi/2:0.00001:pi/2;
    OD=8.93;  ID=2.69; ro=OD/2; ri=ID/2;
    inso= 7.94; insi= 6.35;
    scale=ceil(inso)+1;
    for u=1:length(theta)
        xp1(u)=inso*cos(theta(u)); yp1(u)=inso*sin(theta(u));
        xp2(u)=insi*cos(theta(u)); yp2(u)=insi*sin(theta(u));
        x1(u)=ro*cos(theta(u)); y1(u)=ro*sin(theta(u));
        x2(u)=ri*cos(theta(u)); y2(u)=ri*sin(theta(u));
        x3(u)=.75*cos(theta(u)); y3(u)=.75*sin(theta(u));
    end
    subplot(1,2,ak),plot(xp1,yp1,'m',xp2,yp2,'m',x1,y1,...
    'b',x2,y2,'b',x3,y3,'r');
    hold on
    ns=[.95 1.05]; ns2=[.975 1.025]; kl=1;
    while kl<length(x)
        x(kl);
        %Air-Insulation Intersection
        ODint=((inso^2)-(x(kl)^2))^0.5;
        axis([0 scale -scale scale])
        subplot(1,2,ak),plot([x(kl) x(kl)],[scale ODint],'k');
```

```
        hold on
        axis equal
        %Line in Poly to Poly-Air Intersection
        theta=acos(x(kl)/ODint);
        thetao=asin(nair*sin(pi/2 - theta)/npoly);
        theta_slope= theta + thetao;
        x4(1)=x(kl); y4(1)=ODint;
        m4=tan(theta_slope);
        out=roots([(m4*m4 + 1) (-2*m4*m4*x4(1) + 2*m4*y4(1))...
         (m4*m4*x4(1)*x4(1) + y4(1)*y4(1)-2*m4*x4(1)*y4(1) -insi*insi)]);
        x4(2)=out(1);
        y4(2)=(insi*insi-x4(2)*x4(2))^.5;
        subplot(1,2,ak),plot(x4,y4,'k'); hold on
        %plot(ns2*x4(2), ns2*y4(2),'g')
        %plot(ns2*x4(1), ns2*y4(1),'g')
        %Line in Air and Air-Glass Intersection
        theta2=atan(y4(2)/x4(2));
        theta_airin=pi-(pi-((theta-theta2)+thetao));
        thetao2=asin(npoly*sin(theta_airin)/nair);
        theta_slope2=theta2 + thetao2;
        x5(1)=x4(2); y5(1)=y4(2);
        m5=tan(theta_slope2);
        out2=roots([(m5*m5 + 1) (-2*m5*m5*x5(1) + 2*m5*y5(1))...
         (m5*m5*x5(1)*x5(1) + y5(1)*y5(1)-2*m5*x5(1)*y5(1) -ro*ro)]);
        x5(2)=out2(2);
        y5(2)=(ro*ro-x5(2)*x5(2))^.5;
        subplot(1,2,ak),plot(x5,y5,'k'); hold on
        %plot(ns*x5(2), ns*y5(2),'g')

        %Line in Glass and Glass-Water Intersection
        theta3=atan(y5(2)/x5(2));
        theta_glassin=pi-(pi-((theta2-theta3)+thetao2));
        thetao3=asin(nair*sin(theta_glassin)/nglass);
        theta_slope3= theta3+ thetao3;
        x6(1)=x5(2); y6(1)=y5(2);
        m6=tan(theta_slope3);
        out3=roots([(m6*m6 + 1) (-2*m6*m6*x6(1) + 2*m6*y6(1))...
         (m6*m6*x6(1)*x6(1) + y6(1)*y6(1)-2*m6*x6(1)*y6(1) -ri*ri)]);
        x6(2)=out3(1);
        y6(2)=(ri*ri-x6(2)*x6(2))^.5;
        subplot(1,2,ak),plot(x6,y6,'k'); hold on
        %plot(ns*x6(1), ns*y6(1),'g')

        %Line in Water to Wick
        theta4=atan(y6(2)/x6(2));
        theta_waterin=pi-(pi-((theta3-theta4)+thetao3));
        thetao4=asin(nglass*sin(theta_waterin)/nfluid(ak));
        if isreal(thetao)==0
            kl=length(x)+1
        end
        theta_slope4= theta4+ thetao4;
        x7(1)=x6(2); y7(1)=y6(2);
        storex(kl)=x6(2);
        m7=tan(theta_slope4);
```

```
        out4=roots([(m7*m7 + 1) (-2*m7*m7*x7(1) + 2*m7*y7(1))...
        (m7*m7*x7(1)*x7(1) + y7(1)*y7(1)-2*m7*x7(1)*y7(1) -.75*.75)]);
        x7(2)=out4(2);
        if isreal(x7(2))==0
            out4=roots([(m7*m7 + 1) (-2*m7*m7*x7(1) + 2*m7*y7(1))...
             (m7*m7*x7(1)*x7(1) + y7(1)*y7(1)-2*m7*x7(1)*y7(1) -ri*ri)]);
            x7(2)=out4(1);
            y7(2)=-(ri*ri-x7(2)*x7(2))^.5;
        else
            y7(2)=(.75*.75-x7(2)*x7(2))^.5;
        end
        subplot(1,2,ak),plot(x7,y7,'k'); hold on
        %plot(ns*x7(1), ns*y7(1),'g')
        kl=kl+1;
    end

    xlabel('mm','FontSize',14)
    ylabel('mm','FontSize',14)
    text(-1.9,0,'Copper','FontSize',14)
    text(-1.9,mean([0.75 ri]),fluid(ak),'FontSize',14)
    text(-1.9,mean([ro ri]),'Glass','FontSize',14)
    text(-1.9,mean([ro insi]),'Air','FontSize',14)
    text(-1.9,mean([insi inso]),'Polycarb','FontSize',14)
    text(-1.9,mean([9 inso]),'Air','FontSize',14)
    axis([-2 2 -2 9])
    set(gca,'LineWidth',2,'FontSize',14')
    hold off
end
% for b=1:length(storex)-1
% diffx(b)=storex(b+1)-storex(b);
% end
% diffx=diffx/(x(2));
% figure(2)
% bar(diffx), ylabel('Fraction of Original Spacing','FontSize',14),...
 xlabel('Line Number','FontSize',14)
 %,title('Spacing at Working Fluid Interface')
% set(gca,'LineWidth',2,'FontSize',14')
```

APPENDIX B

VIDEO POSTPROCESSING CODE

```
=1;
for m=1:10
    file=['Trial' num2str(m)]
    disp(['Start ' datestr(now)])
    test=VideoReader([file,'.mp4']);
    frames=read(test);
    numFrames = get(test, 'NumberOfFrames');
    disp(['Frames loaded ' datestr(now)])
    g=[3:floor(test.FrameRate):numFrames];
    frames=frames(:,:,:,g);
    disp(['Frames processed ' datestr(now)])
    data=load([file,'.mat'],'-ascii');
    t=data(:,1);
    t2=data(:,3); t3=data(:,4);
    disp(['Data loaded ' datestr(now)])
    clear data
    i=1;
    len=min([length(g) length(t)]);
    for i= 1:len
        figure(1)
        hold on
        set(gcf,'MenuBar','none','Position',[0 0 test.Width test.Height],...
        'Units','Pixels')
        axis equal
        axis([0 test.Width -test.Height 0])
        axes('Position',[0 0 1 1])
        image(frames(:,:,:,i))
        text(5,test.Height-15,['t=' num2str(i) 's'],'Fontsize',14);
        text((0.5*test.Width),test.Height-45,...
         ['T= ' num2str(roundn(t3(i),-2)) char(176) 'C'],'Color','red',...
         'FontSize',18,'HorizontalAlignment','Center');
        text((0.5*test.Width),20,...
        ['T= ' num2str(roundn(t2(i),-2)) char(176) 'C'],...
```

```
34          'Color','white','FontSize',18,'HorizontalAlignment','Center');
35          axis('off')
36          img=getframe(gcf);
37          nframes(:,:,:,i)=img.cdata;
38          hold off
39          i=i+1;
40          clf
41      end
42      clear frames
43      clear img
44      disp(['Data Combined ' datestr(now)])
45      for k = 1 : len
46          mov(k).cdata = nframes(:,:,:,k);
47          mov(k).colormap = [];
48      end
49      clear nframes
50      v=VideoWriter([file,'e.mp4'],'MPEG-4');
51      v.FrameRate=2;
52      v.Quality=100;
53      open(v)
54      writeVideo(v,mov)
55      close(v)
56      clear mov
57      clear data
58      clear t
59      clear t1
60      clear t2
61      clear t3
62      disp(['Finished ' datestr(now)])
63      close all
64  end
```

APPENDIX C

MATLAB CODE FOR EXPERIMENTAL REPEATABILITY

```
set(0,'defaultLineLineWidth', 1.5)
close all
dryk=[1,15.3;2,28.6;3,41.7;4,54.1;5,68.2];
dryrep=[1.009,15.439;2.000,28.587;2.999,41.7643;4.003,54.300;5.038,67.015];
dryrep2=[0.999 14.53;2.006 28.07; 3.003 41.38; 3.996 54.14; 5.033 66.52];
dryrep3=[1.037 14.52; 2.008 27.31; 2.986 39.37; 3.974 52.06; 5.016 66.00];
all=[dryk; dryrep; dryrep2; dryrep3];
temp=all(:,2);
pow=all(:,1);
[coeff stats]=polyfit(pow,temp,1);
x=[1 2 3 4 5];
[coeff,stats]=polyfit(pow,temp,1);
[fit,delta]=polyval(coeff,x,stats)
plot(pow,temp,'o',x,fit,'b',x,fit+2*delta,'r--',x,fit-2*delta,'r--')
xlabel('Power (W)','FontSize',14),ylabel('Temperature Difference (K)',...
    'FontSize',16)
set(gca,'FontSize',14,'LineWidth',1.5)
legend('Raw Data','Trendline','95% Confindence Bounds','Location',...
    'NorthWest')
```

BIBLIOGRAPHY

[1] C. Loh, E. Harris, D. Chou, Comparative study of heat pipes performances in different orientations, ... Thermal Measurement and ....
URL http://ieeexplore.ieee.org/xpls/abs{_}all.jsp?arnumber=1412178

[2] C. Zhang, C. Hidrovo, Nanoscale Wicking Structures, ASME 2009 ... (2009) 1–14.
URL http://proceedings.asmedigitalcollection.asme.org/proceeding.aspx?articleid=1630843

[3] Y. Li, H.-f. He, Z.-x. Zeng, Evaporation and condensation heat transfer in a heat pipe with a sintered-grooved composite wick, Applied Thermal Engineering 50 (1) (2013) 342–351. doi:10.1016/j.applthermaleng.2012.07.042.
URL http://linkinghub.elsevier.com/retrieve/pii/S1359431112005704

[4] R. Manimaran, K. Palaniradja, N. Alagumurthi, K. Velmurugan, An Investigation of Thermal Performance of Heat Pipe Using Di-water, Science and Technology 2 (4) (2012) 77–80. doi:10.5923/j.scit.20120204.04.

[5] T. Sukchana, C. Jaiboonma, Effect of Filling Ratios and Adiabatic Length on Thermal Efficiency of Long Heat Pipe Filled with R-134a, Energy Procedia 34 (2013) 298–306. doi:10.1016/j.egypro.2013.06.758.
URL http://linkinghub.elsevier.com/retrieve/pii/S1876610213010011

[6] B. Badran, F. M. Gerner, P. Ramadas, T. Henderson, K. W. Baker, Experimental Results for Low-Temperature Silicon Micromachined Micro Heat Pipe Arrays Using Water and Methanol As Working Fluids, Experimental Heat Transfer 10 (4) (1997) 253–272. doi:10.1080/08916159708946547.
URL http://www.tandfonline.com/doi/abs/10.1080/08916159708946547

[7] A. K. Mozumder, M. S. H. Chowdhury, A. F. Akon, Characteristics of Heat Transfer for Heat Pipe and Its Correlation, ISRN Mechanical Engineering 2011 (2011) 1–7. doi:10.5402/2011/825073.
URL http://www.hindawi.com/isrn/me/2011/825073/

[8] S. Peyghambarzadeh, S. Shahpouri, N. Aslanzadeh, M. Rahimnejad, Thermal performance of different working fluids in a dual diameter circular heat pipe, Ain Shams

Engineering Journal 4 (4) (2013) 855–861. doi:10.1016/j.asej.2013.03.001.
URL http://www.sciencedirect.com/science/article/pii/S2090447913000361

[9] K. a. Triplett, S. M. Ghiaasiaan, S. I. Abdel-Khalik, D. L. Sadowski, Gas-liquid two-phase flow in microchannels part I: Two-phase flow patterns, International Journal of Multiphase Flow 25 (3) (1999) 377–394. doi:10.1016/S0301-9322(98)00054-8.

[10] L. Cheng, G. Ribatski, J. R. Thome, Two-Phase Flow Patterns and Flow-Pattern Maps: Fundamentals and Applications, Applied Mechanics Reviews 61 (5) (2008) 050802. doi:10.1115/1.2955990.

[11] C. Y. Yang, C. C. Shieh, Flow pattern of air-water and two-phase R-134a in small circular tubes, International Journal of Multiphase Flow 27 (7) (2001) 1163–1177. doi:10.1016/S0301-9322(00)00070-7.

[12] J. W. Coleman, S. Garimella, Characterization of two-phase flow patterns in small diameter round and rectangular tubes, International Journal of Heat and Mass Transfer 42 (15) (1999) 2869–2881. doi:10.1016/S0017-9310(98)00362-7.

[13] K. Mishima, T. Hibiki, Some characteristics of air-water two-phase flow in small diameter vertical tubes, International Journal of Multiphase Flow 22 (4) (1996) 703–712. doi:10.1016/0301-9322(96)00010-9.

[14] J. E. Julia, B. Ozar, A. Dixit, J.-J. Jeong, T. Hibiki, M. Ishii, Axial Development of Flow Regime in Adiabatic Upward Two-Phase Flow in a Vertical Annulus, Journal of Fluids Engineering 131 (2) (2009) 021302. doi:10.1115/1.3059701.

[15] NIST Webbook: Water (2011).
URL http://webbook.nist.gov/cgi/cbook.cgi?ID=7732-18-5

[16] The Dow Chemical Company: Isopropanol (2012).
URL http://msdssearch.dow.com/PublishedLiteratureDOWCOM/dh{_}08ac/0901b803808aca73.pdf?filepath=oxysolvents/pdfs/noreg/327-00031.pdf

[17] J. Davis (Ed.), ASM Specialty Handbook: Copper and Copper Alloys, ASM International, 2001.

[18] D. Halliday, R. Resnick, J. Walker, Fundamentals of Physics, 10th Edition, Wiley, 2013.